Ore Geology Reviews 163 (2023) 105769

Contents lists available at ScienceDirect

Ore Geology Reviews

journal homepage: www.elsevier.com/locate/oregeorev

Trace-element analysis and radiometric dating by inductively coupled plasma–tandem mass spectrometry: Approaches and applications to metallogeny

Qian Ma [a], Zhiming Yang [a,*], Yueheng Yang [b,*], Zhuyin Chu [b]

[a] Institute of Geology, Chinese Academy of Geological Sciences, Beijing 100037, China
[b] State Key Laboratory of Lithospheric Evolution, Institute of Geology and Geophysics, Chinese Academy of Sciences, Beijing 100029, China

ARTICLE INFO

Keywords:
Metallogeny
(LA)–ICP–MS/MS
Spectral interference
Ultra-trace element analysis
Radiometric dating

ABSTRACT

Inductively coupled plasma–tandem mass spectrometry (ICP–MS/MS) has rapidly established itself as a method for interference-free trace-element and isotope ratio analyses and has broad applications in geochemistry and geochronology, which are essential for understanding ore formation processes and the source of fluids and metals. Connect ICP–MS/MS to a laser ablation (LA) system, *in situ* interference-free trace-element data from ore and gangue minerals can be obtained, providing an effective vector approach to mineral exploration. LA–ICP–MS/MS also provides an unprecedented method for *in situ* dating of β-decay radiogenic isotope systems, which have isobaric interferences between daughter and parent isotopes that mean their ratios cannot be measured using a single quadrupole ICP–MS. In this review, we elucidate the main differences between single quadrupole ICP–MS and ICP–MS/MS, and describe the different approaches (on-mass and mass-shift) that allow interference-free analyses. We review advances in ICP–MS/MS methodology for trace-element (mainly REEs, noble metals and halogens) analyses and laser-based *in situ* U–Pb (with ^{204}Pb correction), ^{87}Rb–^{87}Sr, ^{176}Lu–^{176}Hf, and ^{187}Re–^{187}Os dating of minerals based on publications from January 2012 to July 2023. We also speculate on future applications of the LA–ICP–MS/MS technique in metallogeny.

1. Introduction

Geochemistry plays an essential role in understanding the processes that produce economic concentrations of minerals, whether by hydrothermal, magmatic, metamorphic, hydrologic (both surficial and subsurface), or weathering processes or a combination of these (Hedenquist and Lowenstern, 1994; Groves et al., 1998; Richards, 2003; Sillitoe, 2010; Weis et al., 2012; Zhou et al., 2020). Geochemistry also contributes importantly to a vector approach to exploration when trace-element distributions vary systematically within a mineral system (Hawkes and Webb, 1962; Kelley et al., 2010; Cooke et al., 2020; Wilkinson et al., 2020; Layton-Matthews and McClenaghan, 2022). Obtaining the variations in different trace-element contents within ore and gangue minerals can be particularly valuable for understanding ore formation processes.

Geochronology is also necessary for a complete understanding and quantification of the geologic processes that form mineral deposits, which is essential for constructing reliable genetic models of their formation (Chiaradia et al., 2014). Radiometric dating is one of the methods to determine the time scale of metallic mineral deposit, providing direct ages of minerals formed during different stages of the mineralization process. The ^{87}Rb-^{87}Sr, ^{176}Lu-^{176}Hf and ^{187}Re-^{187}Os β-decay geochronological techniques are well-established dating tool and have been applied widely to the geochronology of mineral systems. Historically, these techniques require analyses of bulk samples where parent isotopes must be separated from decay-product daughter isotopes after dissolution, followed by thermal-ionization mass spectrometry (TIMS) or multi-collector-inductively coupled plasma-mass spectrometry (MC–ICP–MS) isotopic measurements, which can be time consuming and costly, meaning that large quantities of age data can be difficult to obtain. In addition, the requirement for chemical separation of isotopes hinders the acquisition of spatially resolved isotopic ratios.

Many geochemical and geochronological studies of ore deposits have been facilitated by advances in the development of quadrupole (Q)–ICP–MS for quantitative trace-element, ultra-trace-element, and isotope analysis (Bierlein, 1995; Zwahlen et al., 2014; O'Brien et al., 2015; Song et al., 2019; Zhao et al., 2021). The advantages of Q–ICP–MS include

* Corresponding authors.
E-mail addresses: zm.yang@hotmail.com (Z. Yang), yangyueheng@mail.iggcas.ac.cn (Y. Yang).

https://doi.org/10.1016/j.oregeorev.2023.105769
Received 9 August 2023; Received in revised form 3 November 2023; Accepted 4 November 2023
Available online 7 November 2023

parts per trillion levels of detection for elements across the periodic table (from Li to U), a wide linear dynamic range (sub ppt to thousands of ppm), high throughput, and multi-element/isotope capability (Brenner and Taylor, 1992; Becker, 2005). When combined with a laser ablation (LA) system, ICP–MS can provide trace-element contents and U–Pb age information from single crystals of minerals including zircon, apatite, and other U-bearing minerals (Liu et al., 2013; Chew et al., 2014; Cook et al., 2016). However, ICP–MS also has some drawbacks, with the occurrence of spectral interferences being the most important (Dams et al., 1995; Lum and Leung, 2016). For elements affected by interference from argides, chlorides, hydrides, oxides, or matrix elements, detection limits are always high, and trace levels cannot be accurately measured. In addition, *in situ* radiometric dating of β-decay systems cannot be achieved using single quadrupole LA-ICP-MS, as β-decay systems naturally have isobaric interference between the daughter and parent isotopes.

In 2012, the introduction of quadrupole-based ICP–tandem mass spectrometry (ICP–MS/MS), also known as triple quadrupole ICP–MS or ICP–QQQ, has enhanced the concept of chemical resolution to avoid spectral overlap by improving control over reaction cell chemistry. Three years later, Balcaen et al. (2015) reviewed the use of ICP–MS/MS for interference-free quantitative determination of metals and metalloids (including B, C, Al, P, S, Cl, Si, Ti, Cr, Co, Ni, As, Se, Sr, I and Cs) in different sample types (e.g., food, environmental, clinical, biological, and geological materials) by early users of the novel technique and discussed possible reaction pathways with typical reaction gases (e.g., H_2, O_2, and NH_3). Other review articles on ICP-MS/MS including the method development for interference-free ultra-trace element determination (Bolea-Fernandez et al., 2017) and advances in the development and application of ICP–MS/MS in biological, environmental, food, medical, material and radionuclide (Diez-Fernandez et al., 2020; Zhu et al., 2021). In addition, the LA-ICP-MS/MS technique has been successfully applied to *in situ* Rb–Sr, Lu–Hf, K–Ca and Re–Os dating of geological samples and has improved U–Pb dating by removing the ^{204}Hg interference from ^{204}Pb. According to the best of the authors' knowledge, the advances in the development and application of LA-ICP-MS/MS dating of β-decay systems have not been reviewed so far.

This contribution aims to describe the particularities of ICP–MS/MS instruments and the different modes that provide interference-free conditions as well as to provide an overview of advances in (LA)–ICP–MS/MS for trace-element analysis and laser-based *in situ* dating of β-decay systems. We focus on the ultra-trace-element analysis of rare earth element (REE), noble metal, halogen and sulfur contents that aid the petrogenetic interpretation of magmatic–hydrothermal ore deposits, and *in situ* ^{87}Rb–^{87}Sr, ^{176}Lu–^{176}Hf, and ^{187}Re–^{187}Os dating of ore and gangue minerals. We also speculate on future developments and new applications.

2. ICP–tandem mass spectrometry (ICP–MS/MS)

2.1. Instrument setup

Currently available ICP–MS/MS instruments include the Agilent 8800 (2012) and 8900 (2016), the Thermo Fisher Scientific iCAP TQ (2017), and the PerkinElmer NexION 5000 (2020). The main difference with traditional collision reaction cell (CRC)–ICP–MS systems is the introduction of an additional quadrupole (Q1) in front of the CRC (Fig. 1). The ICP–MS/MS instrument can be used in different modes depending on the nature of the analyte, matrix composition, detection limits, and sensitivity required. The instrument can be used as a conventional Q–ICP–MS instrument, with the first quadrupole Q1 operated as an ion guide (no mass selection) and the CRC under vacuum. This mode has the highest sensitivity but cannot accurately determine the contents of elements (e.g., K, Ca, Fe, Ti, V, As, and Se) that are affected by polyatomic interference.

In addition, the CRC can be pressurized with a reactive or non-reactive gas, with Q1 still set for no mass selection (single quad mode). The addition of a non-reactive gas (e.g., He) in the cell can lead to a large reduction in polyatomic interference through kinetic energy discrimination (KED). Polyatomic ions have a larger collisional cross-section than atomic ions with the same mass, thus they collide more frequently and lose more energy than the target ions and can be selectively prevented from entering the MS using a decelerating potential (Feldmann et al., 1999a, Feldmann et al., 1999b). This mode has the additional benefit of reducing the response from low mass, high concentration elements in geological samples (including Na, K, Ca, and Mg) by an order of magnitude or more. This means that elements that would normally require the use of ICP–OES can be included in the ICP–MS run, significantly reducing the cost of analysis per sample. However, some analytes, sample types, and interferences cannot be adequately addressed using collision mode. Examples include trace-level measurement of Si, P, and S and the resolution of doubly charged and isobaric interferences. Although the addition of a reactive gas (e.g., H_2, NH_3, or O_2) in the cell in single quad mode can remove some polyatomic and doubly charged interferences, the formation of unwanted ions in the cell can lead to new interferences—a weak point of single quad mode.

The MS/MS reaction mode is often more efficient than single quad mode, especially for some key elements (e.g., Se, P, S and noble elements) when aiming for ultra-trace-level analysis. In this mode, Q1 can be used as a mass filter, thereby only allowing ions with one m/z ratio to enter the cell. This leads to better control over the reactions taking place in the CRC and more insight into the reactions and origin of the ions

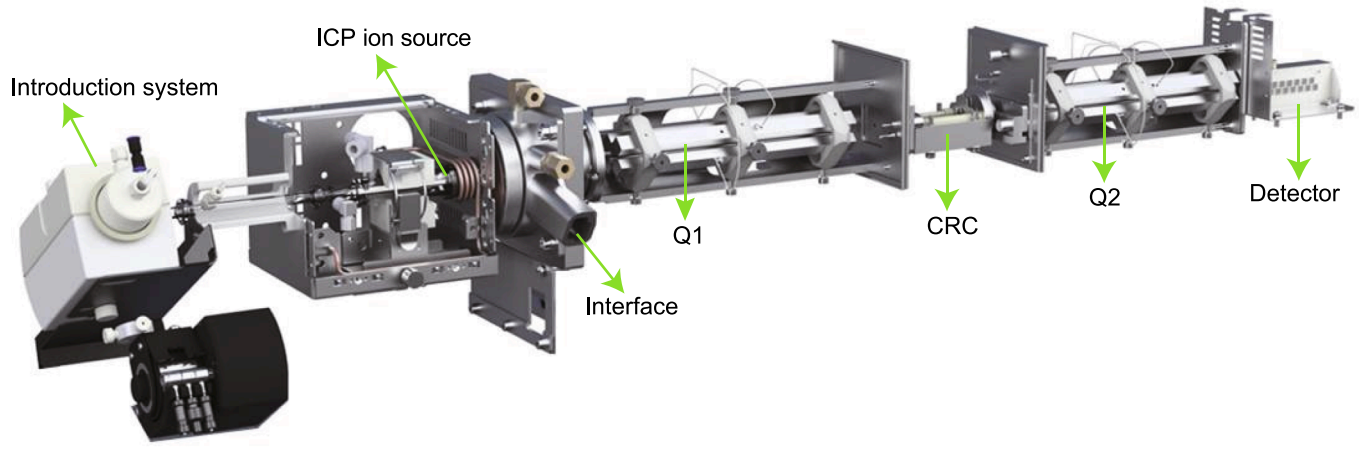

Fig. 1. Schematic of an ICP–MS/MS system with an octupole CRC between two quadrupoles (Agilent Technologies manual).

produced. With chemical resolution based on ion–molecule reactions in CRC, spectral overlap from both atomic and molecular ions with the same *m/z* ratio as the target ion can be removed.

In Fig. 2, an example of the determination of Se contents using different analytical modes and in the presence of different matrix elements (e.g., REEs, Zr, Mo, and Ru) that could lead to interference is shown. With a non-reactive gas (He), only interference by polyatomic ions can be reduced, whereas the doubly charged Gd^{2+} and Dy^{2+} ions cannot be removed (Fig. 2a). Conversion of Se^{+} into SeO^{+} in single quad mode and detection of *m/z* ratios of 96 can solve the problems of both polyatomic and doubly charged ions, but if Zr, Mo, or Ru are present in the samples, erroneous results may be produced (Fig. 2b). However, in MS/MS mode, with the first quadrupole operated as a mass filter, interference-free analysis can be performed, regardless of the matrix composition (Fig. 2c).

An additional advantage of ICP–MS/MS is the improved abundance sensitivity. The International Union of Pure and Applied Chemistry (IUPAC) defines abundance sensitivity in mass spectrometry as the ratio of the maximum ion current recorded at mass (m) to the ion current arising from the same species recorded at an adjacent mass, m ± 1 (IUPAC, 2014). This becomes crucial when low-abundance isotopes have to be measured in the presence of neighboring high-abundance isotopes (e.g., for ultra-trace analysis of high purity materials). Quadrupoles typically used in ICP–MS instruments have abundance sensitivities of 10^{-6}–10^{-7} (Boulyga and Becker, 2002); however, ICP–MS/MS instruments operating in MS/MS mode perform two mass selections using two quadrupole mass spectrometers, and the final abundance sensitivity can be calculated as the product of their corresponding abundance sensitivities and the combined abundance sensitivity for ICP–MS/MS is theoretically 10^{-12}–10^{-14}. An illustrative example of this was presented by Diez Fernández et al. (2015), who reported the use of the technique for determining B/Ca ratios in natural biogenic carbonates. The addition of O_2 to the reaction cell greatly reduced the overlap between the tail of the large ^{12}C signal and the low ^{11}B signal owing to the higher abundance sensitivity of the instrument.

2.2. Overcoming spectral overlap: On-mass and mass shift approaches

With a reactive gas, spectral overlap can be reduced in two different ways: reactions can be induced to convert the interfering species into new species that do not interfere with the measurement of the target ion at its "natural" isotopic mass (on-mass mode), or the target ion can be converted to a product that can be measured free from interference at another *m/z* ratio (mass-shift mode). For example, Pt can be analyzed using two different reactive gases: O_2 and NH_3 (Kutscher et al., 2018). With O_2 in the CRC, Pt will pass through the cell unaffected, as no reaction occurs between Pt and O_2, and it can be detected in on-mass mode (Fig. 3a). The interfering species, HfO^{+}, initially has the same *m/z* ratio as Pt but is converted into HfO_2^{+} and eliminated by the analyzing quadrupole (Q2). At the same time, the first quadrupole (Q1) filters out all ions with lower and higher masses that could potentially react and overlap with the target ion mass. With NH_3 in the CRC (Fig. 3b), Pt undergoes different reactions forming Pt–NH_3 complexes, the most abundant of which is $Pt(NH_3)_2$, leading to a mass shift of 34 amu. HfO^{+} will not react in the same way and will again be eliminated by the analyzing quadrupole. Similar reaction schemes can be applied to other

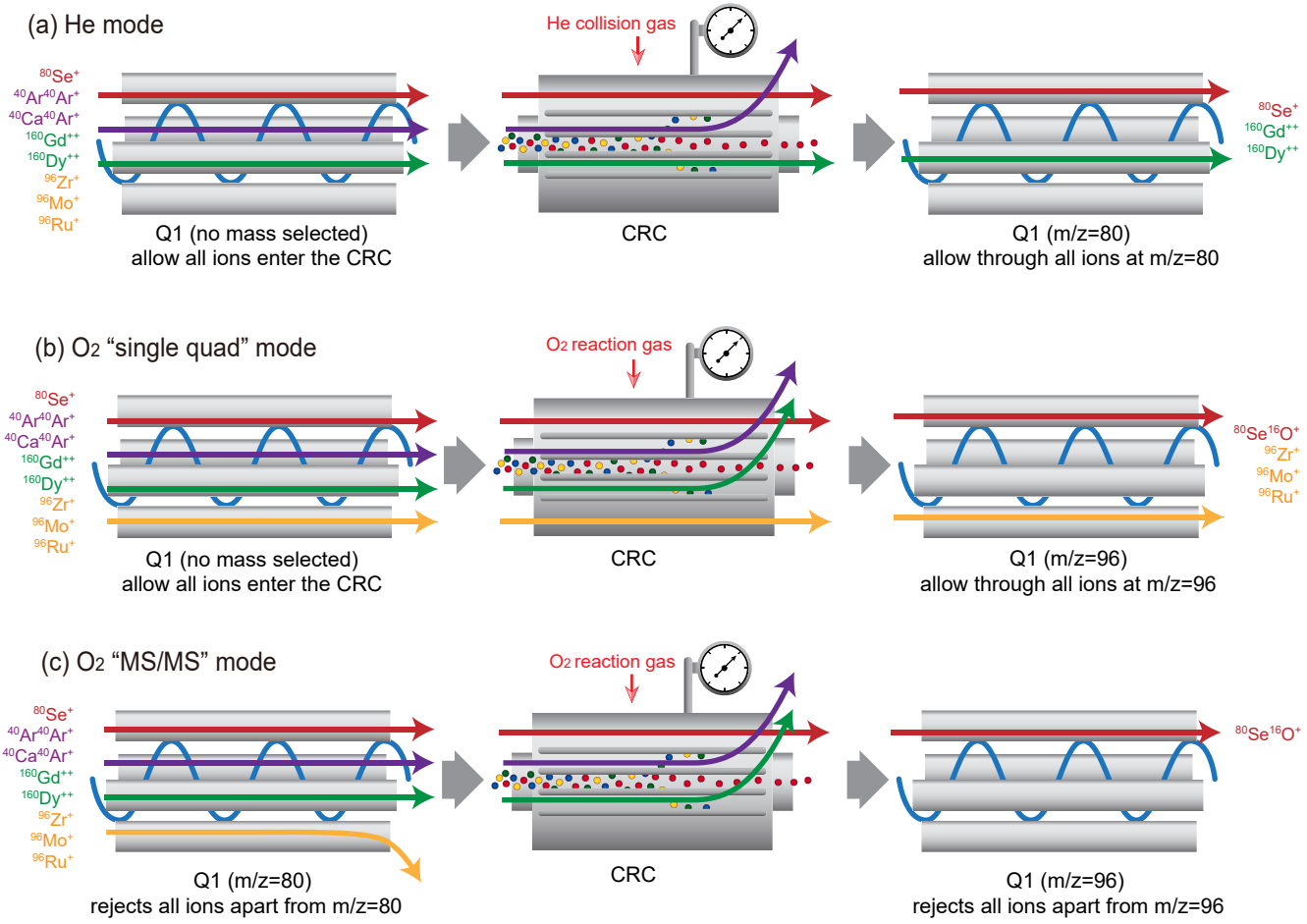

Fig. 2. Analysis of Se in a complex matrix using different modes of an ICP–MS/MS instrument. With Q1 used as an ion guide only (no mass selection), interference remains, whereas operating in MS/MS mode allows interference-free measurement of Se when using O_2 as a reaction gas.

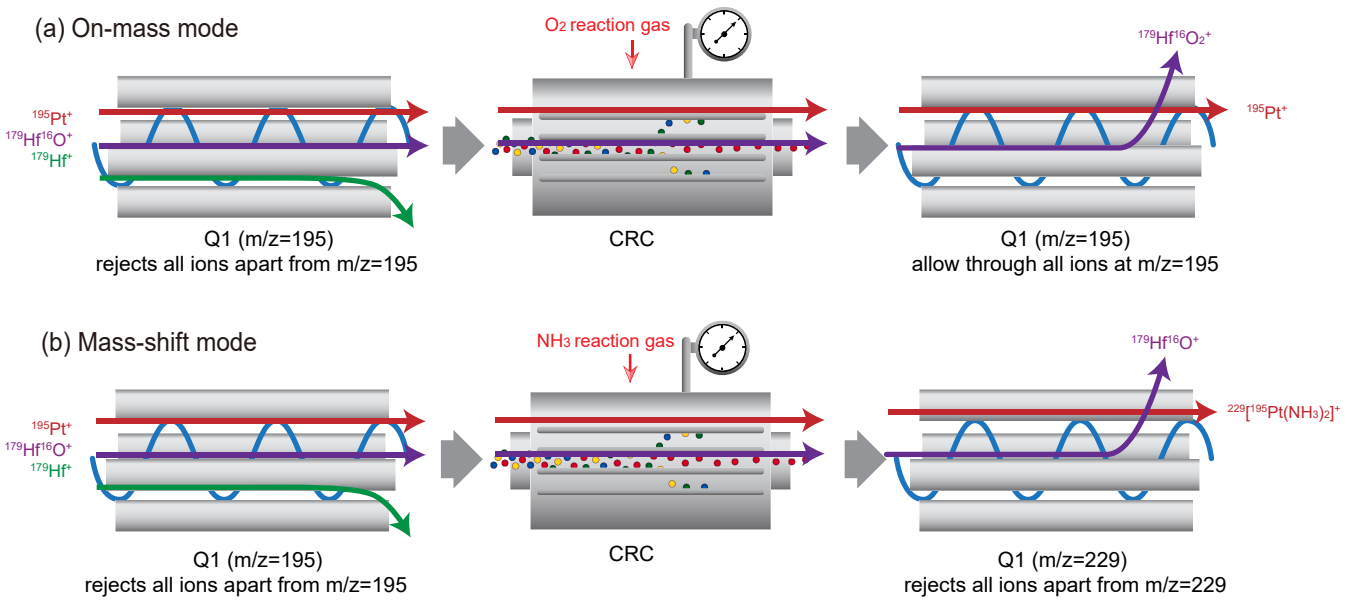

Fig. 3. Illustration of the (a) on-mass and (b) mass shift methods to remove $^{179}Hf^{16}O^+$ interference on $^{195}Pt^+$ (modified after Balaram, 2021).

platinum group elements (PGEs), including Rh, Pd, Ir, as well as Au. In most cases, they do not react with O_2, and the interfering ions can be eliminated efficiently.

2.3. Selection of collision/reaction gas

The first step in method development is the selection of the most appropriate reaction gas. For several elements and matrices, suitable methods have been described in the literature, the instrument manual, or online software provided by the instrument manufacturer. Helieum (He) gas is widely used as a collision gas, and O_2, H_2, NH_3, N_2O, CH_4, and CH_3F are the most used reaction gases (Bolea-Fernandez et al., 2015). Promising results have also been presented using other reaction gases, including CO_2 (Amr et al., 2017) and H_2S (Zhu et al., 2018).

From an analytical standpoint and for new applications, access to information about the mechanisms and efficiencies of reactions between target or interfering elements and possible reaction gases is useful. Typically, the most favorable reactions that take place in a reaction cell are those that do not require additional energy (i.e., exothermic reactions [$\Delta H_r < 0$]), or more accurately those that are thermodynamically permissible ($\Delta G < 0$; Tanner et al., 2002). Several systematic studies of product ion formation over much of the periodic table have been explored with different gases, including O_2, H_2, NH_3, N_2O, CH_3F, H_2S, and CO_2, using commercial ICP–MS/MS systems (Balcaen et al., 2013; Bolea-Fernandez et al., 2014; Sugiyama and Nakano, 2015; Zhu, 2018; Harouaka et al., 2021, Harouaka et al., 2022). These studies are especially useful for the identification of targeted reactions to be leveraged for analytical method development, including for the separation of isobaric interferences from elements of interest. For example, Harouaka et al. (2021) explored ion/molecule reactivity based on thermodynamics across the periodic table using N_2O and an Agilent 8900 ICP–MS/MS. Comparison between the results using N_2O and similar measurements conducted with O_2 show that N_2O is more efficient at forming oxides. Cd^+ and Pb^+ cations produced oxides with N_2O but did not react with O_2. With N_2O in the CRC, when collisions were reactive, two significant species were formed: oxides and nitrides. Oxides (MO^+) were the dominant product, accounting for < 85 % of all product ions, whereas the nitrides (MN^+) accounted for < 20 % of all products. This is because oxide formation, which requires breaking the NN–O bond (1.7 eV), is more energetically favorable than nitride formation, which breaks the N–NO bond (5.0 eV; Armentrout et al., 1982). In addition, for a given tuning, Sr, Ba, and REEs are more reactive and form MO^+ signals accounting for > 50 % of the total signal intensities of all other ions containing that element (e.g., M^+, MN^+, MO^+, MNO^+). However, Na, Ka, Rb, Cs, Cu, Ag, Ga, and Tl hardly react with N_2O, and the MO^+ ions produced are < 1 % of the total signal intensity. Based on this information, a strategy for the use of a specific gas and the conditions needed to enable interference-free measurements can be designed.

3. Approaches

In this section, the analytical methods described in the literature are summarized, focusing on ore-related trace elements and radiometric dating. Analytical approaches for trace elements (including REEs, noble metals, halogens, S, P, etc.) and radiometric dating based on ICP-MS/MS technique are summarized in Tables 3 and 4, respectively.

3.1. Elemental analysis by ICP–MS/MS

3.1.1. Rare earth elements

REEs, which comprise fifteen lanthanides and yttrium, are important tracers of the source of ore-forming fluids, magma and the process of hydrothermal mineralization (Bi et al., 2002; van Doncen et al., 2010; Cao et al., 2021; Rieger et al., 2022). However, the accurate determination of REE contents can be affected by the formation of polyatomic species in the plasma source. Spectral interferences on REEs are summarized in Table 1. Most interferences are BaH^+ on La^+, BaO^+ on Eu^+, SnO^+ on LREEs$^+$ and $SnCl^+$, $BaCl^+$ on HREEs$^+$. Furthermore, some LREE oxide interference can occur owing to the high reactivity of REEs with O_2, which can affect the accurate determination of HREE contents (e.g., interference of $^{143}Nd^{16}O^+$ on $^{159}Tb^+$ and $^{144}Sm^{16}O^+$ on $^{160}Dd^+$). With the ICP-MS/MS instrument, these interferences can be minimized.

Wu et al. (2016) proposed an ICP-MS/MS method for determination of Eu^+ in barium carbonate ($BaCO_3$) materials. Compared with conventional single quadrupole ICP-MS, both NH_3 on-mass mode and O_2 mass shift mode in ICP-MS/MS can be used to effectively eliminate polyatomic interferences, particularly Ba-based interferences. The proposed ICP-MS/MS method is a sensitive technique with a limit of detection as low as 2.0 ng/L for $^{153}Eu^+$. Amr et al. (2017) determined REE contents in plant and soil samples using an Agilent 8800 ICP–MS/MS with O_2 as the reaction gas, and REE oxide contents were measured using the mass-shift strategy, which significantly reduced polyatomic

Table 1
Spectral interferences on isotopes of rare earth elements.

m/z	Isotope abundance (%)								Interference					
	La	Ce	Pr	Nd	Sm	Eu	Gd		Atomic	Dimer	Argide	Chloride	Hydride	Oxide
136		0.19							Xe, Ba	ZnZn	ZrAr, MoAr, RuAr	TcCl, RuCl	BaH	SeO, TeO
137														
138	0.09	0.25							Ba	ZnZn, GaGa	MoAr, RuAr, PdAr	RuCl, RhCl	BaH	SnO, SbO, TeO
139	99.91										TcAr, RuAr, RhAr	RuCl, PdCl	BaH	SbO, TeO
140		88.45								GaGa, GeGe	MoAr, RuAr, PdAr	RhCl, PdCl	BaH, LaH	SnO, SbO, TeO, XeO
141			100								RuAr, RhAr, PdAr	RuCl, PdCl, CdCl	CeH	SbO, TeO
142		11.11		27.2						GaGa, GeGe	RuAr, PdAr	PdCl, AgCl	PrH	TeO, XeO
143				12.2						GeGe	RhAr, PdAr, AgAr	PdCl, CdCl	CeH, NdH	TeO, IO
144				23.8	3.07					GeGe	RuAr, PdAr	AgCl	NdH	TeO, IO, XeO
145				8.3						GeGe	PdAr, AgAr	PdCl, CdCl	NdH, SmH	IO, XeO
146				17.2						GeGe	PdAr, CdAr	AgCl, CdCl	NdH	XeO, BaO
147					14.99					GeGe	AgAr, CdAr	PdCl, CdCl	NdH	XeO
148				5.7	11.24					GeGe	PdAr, CdAr	CdCl, InCl	NdH, SmH	XeO, BaO
149					13.82							CdCl, SnCl	NdH, SmH	XeO, CsO
150				5.6	7.38					GeGe, AsAs	PdAr, CdAr	CdCl, InCl	NdH, SmH	XeO, CsO, BaO
151						47.81				SeSe	CdAr, InAr	CdCl, SnCl	NdH, SmH	CsO, BaO
152					26.75		0.2			SeSe	CdAr, SnAr	InCl, SnCl	EuH	XeO, BaO, CeO
153						52.19				SeSe	CdAr, InAr	CdCl, SnCl	SmH, EuH, GdH	BaO
154					22.75		2.18			SeSe	CdAr, SnAr	SnCl	EuH	BaO, LaO, CeO
155							14.8			SeSe	InAr, SnAr	SnCl, TeCl	SmH, EuH, GdH	BaO, LaO
	Isotope abundance (%)								Interference					
	Gd	Tb	Dy	Ho	Er	Tm	Yb	Lu	Atomic	Dimer	Argide	Chloride	Hydride	Oxide
156	20.47		0.06							SeSe	CdAr, SnAr	SnCl, SbCl	SmH, GdH	BaO, LaO, CeO
157	15.65									SeSe	SnAr, SbAr	SnCl, TeCl	GdH, DyH	LaO, CeO, PrO
158	24.84		0.09							SeSe, BrBr	SnAr, TeAr	SbCl, TeCl	GdH	CeO, PrO, NdO
159		100								SeSe	SnAr, SbAr	SnCl, TeCl	GdH, DyH	CeO, PrO, NdO
160	21.86		2.33							SeSe, BrBr	SnAr, TeAr	SbCl, TeCl	GdH, TbH	CeO, NdO, SmO
161			18.89								SbAr, TeAr	SnCl, TeCl, XeCl	GdH, TbH, DyH	NdO
162			25.47		0.14					SeSe, BrBr, KrKr	SnAr, TeAr	TeCl, ICl	GdH, DyH	NdO
163			24.9							KrKr	SbAr, TeAr, IAr	TeCl, XeCl	DyH, ErH	NdO, SmO
164			28.26		1.6					KrKr	SnAr, TeAr, XeAr	ICl, XeCl	DyH, ErH	NdO, SmO
165				100						KrKr	TeAr, Iar, XeAr	TeCl, XeCl, BaCl	DyH, ErH	NdO, SmO
166					33.5					KrKr	TeAr, XeAr	XeCl	DyH, HoH	NdO, SmO
167					22.87					KrKr	IAr	TeCl, XeCl, BaCl	HoH, ErH	SmO, EuO
168					26.98		0.13			KrKr, SrSr	TeAr, XeAr	XeCl, CsCl	ErH	NdO, SmO, EuO, GdO
169						100				KrKr	XeAr, CsAr	XeCl, BaCl	ErH, YbH	SmO, EuO
170					14.91		3.04			KrKr, SrSr	TeAr, XeAr, BaAr	CsCl, BaCl	ErH, TmH	SmO, EuO, GdO
171							14.28			SrSr	XeAr, CsAr, BaAr, CeAr	XeCl, BaCl, CeCl	ErH, TmH, YbH	EuO, GdO
172							21.83			KrKr, RbRb, SrSr	XeAr, BaAr, CeAr	BaCl	ErH, YbH	SmO, GdO
173							16.13			SrSr	CsAr, BaAr	XeCl, BaCl, LaCl, CeCl	YbH	GdO
174							31.83		Hf	RbRb, SrSr	XeAr, BaAr, CeAr	BaCl, LaCl	YbH	GdO, DyO
175								97.41		SrSr	BaAr, LaAr	BaCl, LaCl, CeCl	YbH, HfH	GdO, TbY

(*continued on next page*)

Table 1 (*continued*)

m/z	Isotope abundance (%)								Interference					
	La	Ce	Pr	Nd	Sm	Eu	Gd		Atomic	Dimer	Argide	Chloride	Hydride	Oxide
176							12.76	2.59	Hf	SrSr	XeAr, BaAr, CeAr	LaCl, PrCl	YbH, LuH	GdO, TbO, DyO

interference on the measurement of REE contents, especially interference from LREE oxides on HREEs. Samples were digested with concentrated acids, and the sample solutions were diluted and measured directly using ICP–MS/MS. The instrumental limits of detection (LODs) ranged from 2.0 to 60 ng/L for all REEs. Zhu et al. (2018) used ICP–MS/MS to determine the Y and La contents in an aqueous Sr and Ba solution. To avoid spectral overlap by $^{88}Sr^{1}H^{+}$ and $^{138}Ba^{1}H^{+}$ on $^{89}Y^{+}$ and $^{139}La^{+}$, respectively, CH_3F gas was added into the reaction cell, which converted the $^{89}Y^{+}$ ions into $(^{89}Y^{19}F_2)^{+}$ and $^{139}La^{+}$ ions into $(^{139}La^{19}F_2)^{+}$, whereas $^{88}Sr^{+}$ and $^{138}Ba^{+}$ did not form $(MF_2)^{+}$ ions. This reduced the LODs for Y and La to 0.42 and 0.09 pg g^{-1}, respectively. Ding et al. (2021) used ICP–MS/MS with O_2 as the reaction gas to determine the distribution of REEs in U ore samples (guilleminite, saléeite, and metatorbernite) after the chemical separation of REEs from the U matrix. The instrumental LODs were 0.11–0.77 pg mL^{-1} for all REEs. Klein et al. (2021) developed an ICP–MS/MS-based multi-element approach targeting the analysis of REEs, Sc, Ga, Ge, Nb, In, Te, and Ta in sediment. N_2O was applied as a reaction gas, which produced more oxides for many TCEs than the frequently used O_2, improving the selectivity and sensitivity of the method and achieving instrument LODs for all analyzed elements of between 0.00023 and 0.13 mg L^{-1}. Furthermore, for all analyzed elements except for Te, the recoveries (or accuracy) from selected reference materials (RMs; marine sediment GBW 07313, sediment GBW 07311, and basalt BCR-2) were between 80 % and 112 %. It is worth noting that the selection of an internal standard to correct for potential matrix effects and instrument instability in ICP–MS/MS should be decided carefully, based on the reactivity of the different analytes and the best reaction products when measuring trace elements (Bolea-Fernandez et al., 2021).

3.1.2. Noble metals

The noble metals comprise the six platinum group elements (PGEs, Ru, Rh, Pd, Os, Ir, and Pt), as well as Au and Ag. These elements typically occur in ore minerals at levels of parts per billion (ng g^{-1}) to a few parts per million (μg g^{-1}). Accurate determination of these metals at trace levels is of interest to the geoscience community and mining industry. The data provide insight into the petrogenesis of rocks and mineral deposits, which is invaluable for exploration studies (Economou-Eliopoulos, 1996; Ismail et al., 2014). The quantification of noble metals in geological samples is most frequently done by ICP–MS. However, interference remains a challenge, as co-existing analyte ions cause isobaric and polyatomic interference on noble metal isotopes, limiting their measurement at low concentrations (Bencs et al., 2003; Barefoot, 2004; Yang et al., 2020). Spectral interferences on noble metals are summarized in Table 2.

ICP–MS/MS has the proven capability for interference-free determination of noble metals in complex matrices. How well different gas modes (including NH_3 and O_2) eliminated interferences on noble metals has been tested, and NH_3 was shown to be the most efficient reaction gas (Sugiyama and Shikamori, 2015). Unlike oxygen, which can only react to form MO^{+} or MO_2^{+}, NH_3 reacts with elemental ions to form a variety of product ions, such as $M(NH)(NH_3)_n^{+}$, $M(NH_2)(NH_3)_n^{+}$ and $M(NH_3)_n^{+}$. This

Table 2
Spectral interferences on isotopes of noble metals.

m/z	Isotope abundance (%)				Interference						
	Ru	Rh	Pd	Ag	Atomic	Dimer	Double-charge	Argide	Chloride	Hydride	Oxide
96	5.54				Zr, Mo	TiTi	Os^{++}, Pt^{++}	FeAr, NiAr	CoCl, NiCl	ZrH, MoH	SeO, BrO, KrO
97											
98	1.87				Mo	TiTi	Pt^{++}, Hg^{++}	FeAr, NiAr	NiCl, CuCl	MoH, RuH	SeO, BrO, KrO
99	12.76				Tc	TiTi	Pt^{++}, Hg^{++}	CoAr, NiAr, CuAr	NiCl, ZnCl	MoH, RuH	SeO, BrO, KrO
100	12.6				Mo	TiTi, VV, CrCr	Hg^{++}	NiAr, ZnAr	CuCl	MoH, TcH, RuH	KrO, SrO
101	17.06					VV	Hg^{++}	NiAr, CuAr	NiCl, ZnCl	MoH, TcH, RuH	KrO, RbO
102	31.55		1.02			VV, CrCr	Hg^{++}, Pb^{++}	NiAr, ZnAr	CuCl, ZnCl,	MoH, RuH	KrO, RbO, SrO
103		100				CrCr	Pb^{++}	CuAr, ZnAr	ZnCl	RuH, PdH	KrO, RbO, SrO
104	18.62		11.14			CrCr	Pb^{++}	NiAr, ZnAr	ZnCl, GaCl	RuH, RhH	KrO, RbO, SrO
105			22.33			CrCr		CuAr, ZnAr, GdAr	ZnCl, GeCl	RuH, RhH, PdH	RbO, SrO, YO
106			27.33		Cd	CrCr		ZnAr, GeAr	GaCl	RuH, PdH	SrO, YO, ZrO
107				51.84		CrCr		ZnAr, GaAr	ZnCl, GeCl	PdH, CdH	ZrO
108			26.46		Cd	CrCr, FeFe		ZnAr, GeAr	GeCl, GaCl	PdH, AgH	ZrO, MoO
109				48.16				GaAr, GeAr	GeCl, SeCl	PdH, AgH, CdH	ZrO, NbO, MoO
110			11.72		Cd	MnMn, FeFe		ZnAr, GeAr, SeAr	GeCl, AsCl	PdH, AgH	ZrO, NbO, MoO
m/z	Isotope abundance (%)				Interference						
	Os	Ir	Pt	Au	Atomic	Dimer	Double-charge	Argide	Chloride	Hydride	Oxide
184	0.02				W	ZrZr		NdAr, SmAr	SmCl	WH	ErO, YbO
185											
186	1.59				W	ZrZr, NbNb		NdAr, SmAr	SmCl, EuCl	WH, ReH	ErO, TmO, YbO
187	1.96				Re	ZrZr, MoMo		SmAr, EuAr	NdCl, SmCl, GdCl	WH, ReH, OsH	ErO, TmO, YbO
188	13.24					ZrZr, MoMo		NdAr, SmAr	EuCl	WH, ReH, OsH	ErO, YbO
189	16.15					MoMo		SmAr, EuAr	SmCl, GdCl	ReH, OsH	YbO
190	26.26		0.014			ZrZr, MoMo		NdAr, SmAr, GdAr	EuCl, GdCl	OsH	YbO, HfO
191		37.3				MoMo		EuAr, GdAr	SmCl, GdCl, DyCl	OsH, PtH	YbO, LuO
192	40.78		0.782			MoMo		SmAr, GdAr	GdCl	OsH, IrH	YbO, LuO, HfO
193		62.7				MoMo		EuAr, GdAr	GdCl, TbCl	OsH, IrH, PtH	YbO, LuO, HfO
194			32.97			MoMo		SmAr, GdAr	GdCl, TbCl	OsH, IrH	YbO, LuO, HfO
195			33.83			MoMo		GdAr, TbAr	GdCl, DyCl	IrH, PtH	HfO
196			25.24		Hg	MoMo		GdAr, DyAr	TbCl, DyCl,	PtH	HfO, TaO, WO
197				100				GdAr, TbAr, DyAr	GdCl, DyCl, ErCl	PtH, HgH	HfO, TaO
198			7.163		Hg	TcTc, RuRu		GdAr, DyAr	DyCl	PtH, AuH	HfO, TaO, WO

Table 3
Overview of analytical methods for measuring trace-element compositions using (LA)–ICP–MS/MS, and applications in the literature.

Analytes	Institute	Instrument	CRC gas	Reaction type [Q1/Q2]	Figures of merit	Applications	References
Rare earth elements							
Eu, Gd, Sm	Zhejiang Institute of Geology & Mineral Resources	Agilent 8800	O_2 or NH_3	Mass-shift [Eu^+/EuO_2^+] or on-mass (NH_3)	ILODs: 2.0 ng/L for $^{153}Eu^+$	Barium carbonate materials	Wu et al., 2016
La, Ce, Pr, Nd, Sm, Eu, Gd, Tb, Dy, Ho, Er, Tm, Yb, Lu	/	Agilent 8800	O_2	Mass-shift [M^+/MO^+]	ILODs: 2.0–60.0 ng/L for all REEs	Plant and soil samples	Amr et al., 2017
Y, La	National Metrology Institute of Japan	Agilent 8800 s	CH_3F	Mass-shift [$M^+/MF2^+$]	ILOD: 0.42 pg g^{-1} for Y; 0.09 pg g^{-1} for La in Sr and Ba matrix	/	Zhu et al., 2018
La, Ce, Pr, Nd, Sm, Eu, Gd, Tb, Dy, Ho, Er, Tm, Yb, Lu	University of South China	Agilent 8900	O_2	Mass-shift [M^+/MO^+]	ILOD: 0.11–0.77 pg mL^{-1} for all REEs	JA-2 (andesite), JB-2 (basalt), JB-3 (basalt) and JR-2 (rhyolite), uranium ore sample	Ding et al., 2021
La, Ce, Pr, Nd, Sm, Eu, Gd, Tb, Dy, Yb, Lu	/	Agilent 8900	N_2O	Mass-shift [M^+/MO^+]	ILODs: 0.00023–0.009 µg L^{-1} for all REEs; recoveries between 80 % and 112 % except Te	Sediment samples	Klein et al., 2021
Noble elements							
Ru, Rh, Pd, Os, Ir, Pt, Au, Ag	Agilent Technologies Japan	Agilent 8800	NH_3	On-mass: Ru, Rh, Pd, Ag; mass-shift: Os, Ir, Pt, Au/[$M + NH_n(NH_3)_m$]	ILODs: 0.0–3.8 pg g^{-1}	/	Sugiyama and Shikamori, 2015
Pd, Pt, Rh	Montanuniversität Leoben	Agilent 8800	NH_3	On-mass: ^{103}Rh; mass-shift: $^{103}Rh/(103/171)$, ^{108}Pd (108/159), ^{195}Pt (195/229)	MLOD: 0.02–0.24 ng g^{-1}	Moss sample	Suoranta et al., 2016
Rh, Pd	Geological Survey of Canada	Laser ablation-Agilent 8800x	NH_3	On-mass	MLOD for ^{103}Rh is 1.7 ng g^{-1}, for ^{105}Pd is 7.0 ng g^{-1}; accuracy: 0.5–19 %; precision: 19–31 %	Cu-rich minerals	Yang et al., 2020
Ru, Rh, Pd, Os, Ir, Pt, Re	Indian Institute of Technology Kanpur	Agilent 8800	NH_3	On-mass	Precision: 0.4–7.7 %	Road dust (BCR-723) and ultramafic komatiite (OKUM)	Mitra et al., 2021
Halogens, S, P and other elements							
B, P, S, Ti, Ca, B/Ca, P/Ca, S/Ca	University of Oviedo	Agilent 8800	O_2	On-mass: B, Ca, Ag; mass-shift [P^+/PO^+, S/SO^+, Ti/TiO^+]	ILOD for B is 0.41 µmol mol-1	Carbonate	Diez Fernandez et al. 2015
P, S, Br, I	/	Thermo Scientific iCAP TQ	O_2	On-mass: ^{127}I; mass-shift [$^{31}P^+/^{31}P^{16}O+$, $^{32}S/^{32}S^{16}O^+$, $^{79}Br/^{79}Br^{16}O^+$]	LODs: 0.064–1.5 ng mL^{-1} with uranium matrix	Uranium ore	Fletcher et al., 2020
F	University of Aberdeen, UK	Agilent 8800	NH_3	Mass-shift [$^{138}Ba^{19}F^+/^{138}Ba^{19}F(^{14}NH_3)_3^+$]	ILODs: 0.043 mg L^{-1}	Fluorine compounds in environmental samples	Jamari et al., 2017
F	China University of Geosciences, Wuhan	Agilent 8800	NH_3	Mass-shift [$^{138}Ba^{19}F^+/^{138}Ba^{19}F(^{14}NH_3)_3^+$]	ILODs: 0.022 µg mL^{-1}	Food and tea samples	Guo et al., 2017
Ge	Macquarie University	Laser ablation-Agilent 8900	N_2O	Mass-shift [Ge^+/GeO^+]	MLOD < 0.2 µg g-1	Ultramafic alkaline rocks	Phillips et al., 2023

ILOD: Instrumental limit of detection.
MLOD: Method limit of detection.

is a potential problem when NH_3 is used in a conventional single quadrupole CRC-ICP-MS as all ions enter the CRC and may react with NH_3 to form new spectral interferences. In contrast, the ICP-MS/MS operating in MS/MS reaction mode can resolve this issue as the first quadrupole selects only the target mass to pass into the cell, so the reaction chemistry is controlled and consistent. Sugiyama and Shikamori (2015)'s study revealed that Ru^+, Rh^+, Pd^+ and Ag^+ had low reaction rates with NH_3, while Os^+, Ir^+, Pt^+ and Au^+ exhibited high reactivity. As for the major interference ions, such as SrO^+, RbO^+, YO^+, LuO^+, YbO^+, ZrO^+, NbO^+, HfO^+, TaO^+ and WO^+ showed high reaction rates with NH_3. Although interference ions also react with NH_3 to form various product ions which may overlap with the mass of the analyte product ion, an analyte product ion that is free (or relatively free) from spectral interference can be found by using a "product ion scan" function of ICP-MS/MS. Finally, Sugiyama and Shikamori (2015) established an on-mass method for the determination of Ru, Rh, Pd and Ag and a mass-shift method for Os, Ir, Pt and Au transferred to $Os(NH)^+$, $Ir(NH)^+$, $Pt(NH_3)_2^+$ and $Au(NH_3)_2^+$. This method successfully measured 1 ng g^{-1} metal contents accurately in a matrix-free standard solution containing interfering elements Cu, Zn, Ni, Mo, Y, Sr, Rb, Zr, Nb, Pb, Hg, Ta, W, Hf, and REEs, demonstrating the effectiveness of the MS/MS reaction cell with NH_3 at removing complex interferences on noble metals (Sugiyama and Shikamori, 2015).

Suoranta et al. (2016) discussed in detail the advantages of MS/MS mode over single MS mode. The PGE mass fractions determined for BCR-723 (road dust RM) in single-MS mode was 20–80 times higher than their certified values. The addition of NH_3 into the CRC and measuring in MS/MS mode significantly reduced interferences, and the measured PGE mass fractions were close to the certified values. The PGE and Re mass fractions in an ultramafic komatiite RM, OKUM, were measured to investigate the reliability of the ICP–MS/MS method proposed by Mitra et al. (2021). The Rd, Pd, Re, and Pt mass fractions measured in OKUM

Table 4
Overview of analytical methods for radiometric dating using LA–ICP–MS/MS.

Minerals	Institute	Laser ablation system	ICP-MS/MS	CRC gas	Reaction type	Laser parameters	Reference materials	Figures of merit	Geological applications	References
U-Pb dating										
Zircon	University of Gothenburg	New Wave NWR213	Agilent 8800	NH_3 + O_2	Mass shift for U (UO^+); Pb on mass; charge-transfer for Hg (Hg^+/Hg^0)	Spot size: 25 μm Repetition rate: 5 Hz Fluence: 7 J cm^{-2}	Plesovice zircon	/	/	Kasapoğlu et al., 2016
Apatite, titanite	University of Adelaide	RESOlution-LR ArF 193 nm	Agilent 8900x	NH_3	Mass shift for U (UNH^+); Pb on mass; charge-transfer for Hg (Hg^+/Hg^0)	Apatite: Spot size: 29 or 43 μm Repetition rate: 5 Hz Fluence: 3.5 J cm^{-2} Titanite:Spot size: 51 μm Repetition rate: 5 Hz Fluence: 5 J cm^{-2}	MAD apatite, MKED1 titanite	/	/	Gilbert et al., 2020
Apatite	University of Gothenburg	ESI NWR213	Agilent 8800	NH_3 + N_2O or NH_3 only	NH3-N2O mode: mass shift for U (UO^+); NH3-only mode: on-mass for U^+; Pb on-mass; charge-transfer for Hg (Hg^+/Hg^0)	40–50 μm laser spot using NH_3-N_2O mode and 65–90 μm laser spot for NH_3-only mode.	MAD2	Age accuracy < 4 %, reproducibility < 2 %	/	Xiang et al., 2021
Rb-Sr dating										
Feldspar, mica, biotite	University of Gothenburg	ESI 213NWR	Agilent 8800	O_2	Mass shift for Sr (SrO^+); Rb on mass	Spot size: 80–110 μm Repetition rate: 10 Hz Fluence: 7 J cm^{-2}	BCR-2G, NIST SRM610 and biotite La Posta	Age accuracy < 1.5 %, initial $^{87}Sr/^{86}Sr$ ratios accuracy < 0.2 %	Magmatic rocks	Zack et al., 2016
Mica	University of Gothenburg	ESI 213NWR	Agilent 8800	N_2O	Mass shift for Sr (SrO^+); Rb on mass	Spot size: 50 μm Repetition rate: 4–5 Hz Fluence: 6 J cm^{-2}	NIST 610, Mica-Mg-NP	Mica isochron age error ~ 1 %	/	Hogmalm et al., 2017
Fluorite, biotite, calcite, epidote, albite, muscovite, adularia	University of Gothenburg	ESI 213NWR	Agilent 8800	N_2O or SF_6	Mass shift for Sr (SrO^+ or SrF^+); Rb on mass	Spot size: 50 μm Repetition rate: 4–5 Hz Fluence: 6 J cm^{-2}	NIST610	/	Vein mineralization	Tillberg et al., 2017
Plagioclase, albite, K-feldspar, muscovite and biotite	University of Gothenburg	ESI 213NWR	Agilent 8800	/	/	/	/	/	Orogenic gold deposit	Şengün et al., 2019
Phlogopite	Macquarie University	LSX213 G2 + 213 nm, analyte G2 ATEX 193 nm ArF excimer.	Agilent 8900	N_2O	Mass shift for Sr (SrO^+); Rb on mass	Spot size: 85 μm Repetition rate: 5 or 10 Hz Fluence: 7 J cm^{-2}	NIST 610, Mica-Mg-NP, and BHVO-2G	/	Kimberlite	Gorojovsky and Alard, 2020
Biotite, phengite, muscovite, apatite,	Curtin University	RESOlution LR 193 nmArF excimer	Agilent 8900	N_2O	Mass shift for Sr (SrO^+); Rb on mass	Spot size: 87 or 64 μm Repetition rate: 5 Hz Fluence: 2.5 J cm^{-2}	NIST 610, Mica-Mg-NP	/	Metamorphic, hydrothermal and mineralization events	Olierook et al., 2020
K-feldspar, illite, calcite and albite	/	/	/	/	/	/	/	/	Slickenfibres in deep crystalline basement faults	Tillberg et al., 2020

(*continued on next page*)

Table 4 (*continued*)

Minerals	Institute	Laser ablation system	ICP-MS/MS	CRC gas	Reaction type	Laser parameters	Reference materials	Figures of merit	Geological applications	References
Biotite, muscovite and feldspars	University of Adelaide	RESOlution-LR ArF 193 nm	Agilent 8900	N_2O	Mass shift for Sr (SrO^+); Rb on mass	Spot size: 87 or 64 μm Repetition rate: 5 Hz Fluence: 3.5 J cm^{-2}	Mica-Mg-NP	/	Archean to Proterozoic crustal evolution	Li et al., 2020
Celadonite	University of Victoria	Teledyne CETAC LSX-213 G2 + Nd:YAG 213 nm	Agilent 8800 #100	10 % CH_3F / 90 % He	Mass shift for Sr (SrF^+); Rb on mass	Spot size: 50 μm Repetition rate: 10 Hz Fluence: 6 J cm^{-2}	NIST 610, Mica-Mg-NP	/	Dating upper ocean crust lavas	Laureijs et al., 2021
Phlogopite	University of Adelaide	RESOlution ArF (193 nm) excimer and NWR (213 nm) Nd-YAG	Agilent 8900	N_2O	Mass shift for Sr (SrO^+); Rb on mass	Line raster: Spot size 74 μm Repetition rate 5 Hz Fluence: 3.5 J cm^{-2} Spot: 74 μm, 5 Hz, 10 J cm^{-2}	NIST 610, Mica-Mg-NP	Age accuracy < 3 % for 70 % of analyzed samples	/	Redaa et al., 2021
Illite, K-feldspar, albite, calcite, mica, zeolites, fluorite and/or epidote	University of Gothenburg, Sweden	ESI 213NWR	Agilent 8800	N_2O or SF_6 + H_2	Mass shift for Sr (SrO^+ or SrF^+); Rb on mass	Spot size: 50–80 μm	NIST 610, Mica-Mg-NP	/	Poly-phased vein mineralization	Tillberg et al., 2021
Biotite	Guangzhou Tuoyan Analytical Technology, China.	NWR193 ArF	iCAP TQ 00108	N_2O	Mass shift for Sr (SrO^+); Rb on mass	Spot size: 110 μm Repetition rate: 5 Hz Fluence: 7 J cm^{-2}	Mica-Mg-NP	/	Metamorphic evolution of North Himalayan gneiss domes	Gou et al., 2022
Biotite	Curtin University	RESOlution LR 193 nm ArF	Agilent 8900	N_2O	Mass shift for Sr (SrO^+); Rb on mass	Spot size: 64 μm Repetition rate: 5 Hz Fluence: 2.5 J cm^{-2}	NIST 610, Mica-Mg-NP	/	Lithological fabric	Liebmann et al., 2022
NPs of GL-O (glauconite), Mica-Mg (phlogopite), Mica-Fe (biotite) and FK-N (K-feldspar)	University of Adelaide	RESOlution LR 193 nm ArF	Agilent 8900	N_2O	Mass shift for Sr (SrO^+); Rb on mass	Spot size: 74 or 67 μm Repetition rate: 5 Hz Fluence: 3.5 J cm^{-2}	NIST 610, Mica-Mg-NP	/	/	Redaa et al., 2022a
Muscovite and K-feldspar	University of Adelaide	RESOlution LR 193 nm ArF	Agilent 8900	N_2O	Mass shift for Sr (SrO^+); Rb on mass	Spot size: 74 or 67 μm Repetition rate: 5 Hz Fluence: 3.5 J cm^{-2}	Mica-Mg-NP	/	Tectono-thermal events and mineralization	Redaa et al., 2022b
Biotite, muscovite and Mica-Fe-NP	University of Gothenburg	ESI NWR213	Agilent 8800	N_2O	Mass shift for Sr (SrO^+); Rb on mass	Round laser spots with a diameter of 50 and 60 μm; Rectangular spot was used with a width of 20 μm and length of 80 and 100 μm respectively. Repetition rate: 10 Hz	Mica-Mg-NP	/	Thermochronological and petrochronological studies	Rösel et al., 2022

(*continued on next page*)

Table 4 (*continued*)

Minerals	Institute	Laser ablation system	ICP-MS/MS	CRC gas	Reaction type	Laser parameters	Reference materials	Figures of merit	Geological applications	References
						Fluence: 5–6.8 J cm^{-2}				
Illite	University of Adelaide	RESOlution LR 193 nm ArF	Agilent 8900x	N_2O	Mass shift for Sr (SrO^+); Rb on mass	Spot size: 74 μm Repetition rate: 10 Hz Fluence: 3.5 J cm^{-2}	Mica-Mg-NP	/	Unraveling the histories of Proterozoic shales	Subarkah et al., 2022
Phlogopite, K-richterite, K-feldspar, biotite, clinopyroxene, plagioclase	Macquarie University	Photon Machines Excimer 193 nm	Agilent 8900	N_2O	Mass shift for Sr (SrO^+); Rb on mass	Repetition rate: 5 Hz Fluence: 7 J cm^{-2} Spot size: 85 μm	Mica-Mg-NP and NIST 610, BCR-2G, BHVO-2G	/	Igneous rocks	Wang et al., 2022
Biotite	Northwest University, China	ESI NWR FemtoUC 257 nm	Agilent 8900	N_2O	Mass shift for Sr (SrO^+); Rb on mass	Spot size: 30 μm, line scan, length 60 μm Fluence: 2.5–3.5 J cm^{-2}Frequency: 5–8 Hz	NIST 610	/	Pegmatite	Chen et al., 2023
Muscovite	Curtin University	RESOlution LR 193 nm ArF	Agilent 8900	N_2O	Mass shift for Sr (SrO^+); Rb on mass	/	/	/	Time-strain evolution of shear zones	Ribeiro et al., 2023
Muscovite, biotite	University of British Columbia Okanagan	ESI 193NWR	Agilent 8900	N_2O	Mass shift for Sr (SrO^+); Rb on mass	Spot size: 50 μm Repetition rate: 10 Hz Fluence: 4 J cm^{-2}	NIST 610, Mica-Mg-NP	/	Himalayan mica	Larson et al., 2023
Lu-Hf										
Garnet, apatite and xenotime	University of Adelaide	RESOlution 193 nm	Agilent 8900	10 % NH_3 in 90 % He	Mass shift for Hf [$Hf(NH)(NH_2)(NH_3)_3^+$]; Lu on mass	Spot size: 43–120 μm Repetition rate: 5 Hz Fluence: 3 J cm^{-2}	NIST 610	Age uncertainties ~ 0.5 %	/	Simpson et al., 2021
Apatite	Curtin University	RESOlution 193 nm	Agilent 8900	10 % NH_3 in 90 % He	Mass shift for Hf [$Hf(NH)(NH_2)(NH_3)_3^+$]; Lu on mass	Spot size: 67 μm Repetition rate: 10 Hz Fluence: 3.3 J cm^{-2}	NIST 610, OD306 apatite	/	Thermotectonic history of the Akia terrane	Gillespie et al., 2022
Phosphate (merrillite and stanfieldite)	University of Adelaide	RESOlution LR 193 nm	Agilent 8900x	10 % NH_3 in 90 % He	Mass shift for Hf [$Hf(NH)(NH_2)(NH_3)_3^+$]; Lu on mass	Spot size: 173 and 257 μm	NIST 610, OD306 apatite	/	Space exploration	Glorie et al., 2022
Calcite	University of Adelaide	RESOlution LR 193 nm	Agilent 8900x	10 % NH_3 in 90 % He	Mass shift for Hf [$Hf(NH)(NH_2)(NH_3)_3^+$]; Lu on mass	Spot size: 257 μm Repetition rate: 10 Hz Fluence: 10 J cm^{-2}	NIST 610 and MKED calcite	Age uncertainties of 1.7 %-6% were obtained from calcite with 0.5 ppm Lu concentrations	/	Simpson et al., 2022
Fluorite	University of Adelaide	RESOlution LR 193 nm	Agilent 8900x	10 % NH_3 in 90 % He	Mass shift for Hf [$Hf(NH)(NH_2)(NH_3)_3^+$]; Lu on mass	Spot size:173 or 257 μm Repetition rate: 10 Hz Fluence: 9 J cm^{-2}	NIST 610 and calcite ME-1	/	/	Glorie et al., 2023
Garnet	University of Adelaide	RESOlution LR 193 nm	Agilent 8900x	10 % NH_3 in 90 % He	Mass shift for Hf [$Hf(NH)(NH_2)(NH_3)_3^+$]; Lu on mass	Spot size:43 or 120 μm Repetition rate: 10 Hz Fluence: 3.5 J cm^{-2}	NIST 610	Age precision ~ 1.5 %	Polymetamorphic histories	Simpson et al., 2023

(*continued on next page*)

Table 4 (*continued*)

Minerals	Institute	Laser ablation system	ICP-MS/MS	CRC gas	Reaction type	Laser parameters	Reference materials	Figures of merit	Geological applications	References
Xenotime, apatite	Institute of Geology and Geophysics, Chinese Academy of Sciences	Photon Machines Analyst G2	Thermo Fisher Scientific iCAP TQ	High-purity NH_3	Mass shift for Hf [$Hf(NH)(NH_2)(NH_3)_3^+$]; Lu on mass	Spot size:50–150 μm	NIST 610 and XN02 xenotime	Accuracy of the common-Hf corrected single-spot ages were < 1.5 %, precision of common-Hf corrected single-spot ages were in a range of 1.5–8.1 % and 9.2–36.0 % for xenotime and apatite	/	Wu et al., 2023
Re-Os										
Molybdenite	University of Gothenburg	ESI 213NWR	Agilent 8800	CH_4	Mass shift for Os ($OsCH_2^+$); Re on mass	Spot size: 70 μm Repetition rate: 5 Hz Fluence: 3.1 J cm^{-2}	Moly Hill and Merlin molybdenite NPs	Age accuracy < 1, precision from ~ 1–5 % depending on Re concentration	/	Hogmalm et al., 2019
K-Ca										
Mica	University of Gothenburg	ESI 213NWR	Agilent 8800	SF_6 + H_2	Mass shift for Ca ($^{40}Ca^{19}F^+$)	/	Mica-Mg and BCR-2G	Age precision ~ 2 %	/	Hogmalm et al., 2017

were within error of their consensus values. Using a Thermo Fisher Scientific iCAP TQ ICP–MS/MS, Kutscher et al. (2018) reported the measurement of the Au, Pt, Rh, and Ir mass fractions in the AMIS 0416 ore RM using O_2 on-mass and NH_3 mass-shift modes. The results of both modes agree well with the certified values (recovery = 89 %–107.6 %).

Combining ICP–MS/MS with a laser ablation sample introduction system provides a promising microbeam technique for determining the contents of noble metals with very low limits of detection. Yang et al. (2020) reported the measurement of low ng g^{-1} contents of Rh and Pd in Cu-rich minerals using LA–ICP–MS/MS for the first time. Using He as a collision gas combined with NH_3 as a reaction gas under MS/MS mode, 99.8 % of the CuAr interference was removed and 98 % of the sensitivity remained. The CuAr contribution to ^{103}Rh and ^{105}Pd signals in chalcopyrite and bornite was < 2.3 ng g^{-1}, a reduction of more than two orders of magnitude compared with those obtained using single quadrupole LA–ICP–MS. The method LODs for ^{103}Rh (1.7 ng g^{-1}) and ^{105}Pd (7.0 ng g^{-1}) obtained using LA–ICP–MS/MS with an ablation spot size of 110 μm were an order of magnitude lower than those obtained using single quadrupole LA–ICP–MS (16 ng g^{-1} for Rh and 48 ng g^{-1} for Pd), demonstrating the potential for LA–ICP–MS/MS to be used widely for the quantitative determination of trace PGE contents in Cu-rich sulfide minerals (Yang et al., 2020).

3.1.3. *Halogens, S, P, and other elements*

Halogens and light elements (such as S, B, P, etc.) play an important role during mass transport in mineralizing fluids and magma (Webster and Duffield, 1994); therefore, better constraints on the halogen and light element contents of magmas and associated fluids are of great importance to the understanding of metallogenesis. Halogens, including fluorine (F), chlorine (Cl), bromine (Br), and iodine (I), are typically present as anionic species. It has been shown that using pyrohydrolysis to extract the halogen anions, ion chromatography to separate them, and conductivity detection for analysis is effective, but the detection limits are generally orders of magnitude higher than those obtained using an ICP–MS (Balcone-Boissard et al., 2009).

Due to the excellent interference elimination capability of ICP–MS/MS, the LODs of halogens other light elements could be lowered further, especially for the measurement of these key elements in complex matrices. For example, Fletcher et al. (2020) used ICP–MS/MS to determine P, S, Br, and I contents in U ore contents during research into mine source and production quality. With ICP–MS/MS, no chemical separation is needed before analysis. The method limit of detection for P, S, Br, and I are 3.2, 30, 1.28, and 4.7 ng mL^{-1}, respectively, which have not been undertaken by traditional Q-ICP–MS.

F cannot be directly detected by conventional Q-ICP-MS because of severe water-derived interferences at m/z = 19 from $^1H_3^{16}O^+$ and $^1H^{18}O^+$, and extremely low sensitivity due to the fact that it is very difficult to convert fluorine atoms to the positive ions that are measured in ICP-MS. Yamada (2015) discussed the feasibility of F detection by ICP − MS/MS, where F was changed to BaF^+ through the online addition of barium solution, the formation of polyatomic BaF^+ (at a new mass of m/z = 157, $^{138}Ba^{19}F^+$) ions was enabled and introduced into Q1. With NH_3 in the CRC, $^{138}Ba^{19}F(^{14}NH_3)_3^+$ was the product of mass-shift and measured at Q2. The potential interfering ions with the same m/z, such as $^{138}Ba^{18}O^1H^+$, $^{138}Ba^{16}O^1H_3^+$, and $^{138}Ba^{17}O^2H^+$ can be reduced under MS/MS mode (Guo et al., 2017; Jamari et al., 2017).

In addition, a very low detection limit for B (0.41 μmol mol^{-1}), P and S in natural biogenic carbonates was achieved by ICP–MS/MS, allowing very low B/Ca, P/Ca, and S/Ca ratios to be measured in organic phases, which is of interest for research into ocean acidification but out of reach even for sector field–ICP–MS (Diez Fernández et al., 2015). ICP–MS/MS also provides accurate analysis of low Ge concentrations in silicates and sulfides matrix. The use of LA–ICP–MS/MS with N_2O as a reaction gas to analyze Ge as an oxide in silicates has been proposed by Phillips et al. (2023). Contrary to high mass resolution, this approach does not significantly reduce sensitivity, thus preserving spatial resolution even

for minerals with sub μg g^{-1} levels of Ge.

3.2. Radiometric dating using LA–ICP–MS/MS

3.2.1. U–Pb dating

Solution-based ID–TIMS has successfully produced U–Pb dates with high accuracy and precision, but ID–TIMS is markedly more time-consuming and lacks the high spatial resolution provided by micro-beam methods. LA–ICP–MS U–Pb dating is one of the most commonly used methods for dating minerals, including zircon, apatite, titanite, and calcite with high spatial resolution (20–80 μm). However, many of these U-bearing minerals also contain non-radiogenic common Pb, which must be corrected for to accurately determine the age of the mineral. The direct measurement of ^{204}Pb is theoretically the ideal method for common Pb correction (Petrus and Kamber, 2012), as it does not assume U/Pb concordance. The other advantage of ^{204}Pb corrections is for samples where intercept ages cannot be determined accurately because of multiple age populations (e.g., detrital samples) or samples that exhibit a degree of open-system behavior. However, the measurement of ^{204}Pb by ICP–MS is currently limited by isobaric interference from ^{204}Hg. However, the ^{204}Pb correction was hindered by the inaccurate determination because of ^{204}Hg interference.

ICP–MS/MS can address the previously unresolvable ^{204}Hg interference on ^{204}Pb. Woods (2014) from Agilent Technologies (UK) showed for the first time that using NH_3 in the reaction cell can effectively remove interference from ^{204}Hg to obtain an accurate $^{204}Pb/^{208}Pb$ isotopic measurement by solution ICP-MS/MS, as > 90 % Hg underwent a charge transfer reaction with NH_3 ($Hg^+ + NH_3 = Hg^0 + NH_3^+$), while < 2 % of the Pb reacts with the NH_3. Gilbert and Glorie (2020) extended this method to directly measure ^{204}Pb and subsequent common ^{204}Pb correction in a range of common Pb-bearing apatites and titanites by LA–ICP–MS/MS. For apatites and titanites with ^{204}Pb signal intensities of > 100 cps, the ^{204}Pb-corrected age and lower intercept ages agree within error, indicating the effective of the ^{204}Pb-corrected method. However, for very low ^{204}Pb signal intensities (<20 cps), the uncertainties are too large to produce meaningful corrected ratios. Thus, using as large a beam size as practical and tuning the ICP–MS/MS for maximum sensitivity is essential to minimize the uncertainties on apatite and titanite ages.

Some gases were added to the NH_3 reaction gas in the CRC to improve signal intensity and stability. Kasapoğlu et al. (2016) found that adding O_2 as a second reaction gas leads to the stable production of UO^+ as the dominant U reaction product without compromising Hg removal and Pb transmission. Using this approach, they obtained LA–ICP–MS/MS zircon U–Pb ages of 51.7 ± 4.7 to 47.8 ± 2.4 Ma from basaltic to rhyolitic volcanic rocks in lower Eocene terrestrial sedimentary units in the Central Sakarya Zone. Xiang et al. (2021) used N_2O instead of O_2 as the second gas in the CRC and produced a stable UO^+ signal. They compared this NH_3–N_2O method with using only NH_3, by comparing U–Pb ages of eight apatite RMs with ages ranging from 21 to 1160 Ma. Results show that the measured ages of the apatites were within 4 % of the reference ages, and the accuracy of U–Pb dating is not measurably affected by different reaction gases. Compared with the T-W concordia lower intercept age which was done during classic single quadrupole LA-ICP-MS analysis, the weighted mean ^{204}Pb-corrected $^{206}Pb/^{238}U$ age for both reaction gases of LA-ICP-MS/MS are more accurate within the uncertainty of the ID-TIMS datum.

3.2.2. Rb–Sr dating

The pioneering work of Moens et al. (2001) demonstrated that online separation of ^{87}Sr from ^{87}Rb using CRC technology enables direct dating using a single quadrupole mass spectrometer with a CRC (CRC–ICP–MS). Using CH_3F as a reaction gas, $^{87}Sr^+$ reacts to form $^{87}Sr^{19}F^+$ and can be measured at a *m/z* ratio of 106, whereas $^{87}Rb^+$ is largely unreactive due to its more stable electron configuration and can be measured on-mass. This method was used for the Rb/Sr isochron age determination of magmatic rocks after dissolution of the samples without chromatographic separation. The measured age agrees with the reference age of thermal ionization mass spectrometry (TIMS). However, the precision of the age is relatively poor (up to ~ 11 %), restricting the geological application. A problem with using a single quadrupole CRC–ICP–MS is the new interferences at *m/z* = 106, such as $^{106}Pd+$, $^{90}Zr^{16}O^+$, $^{89}Y^{16}O^1H^+$, $^{66}Zn^{40}Ar^+$, etc. This can be avoided by using ICP–MS/MS under MS/MS mode. Accurate determination of $^{87}Sr/^{86}Sr$ isotopic ratios in BCR-2 and BHVO-2 basalt RMs were measured by Liu et al. (2020) using solution ICP–MS/MS in mass-shift mode with O_2 as the reaction gas, with an external precision of better than 0.1 % relative standard deviation (RSD) without prior Sr purification. Furthermore, Bolea-Fernandez et al. (2016) reported the use of LA–ICP–MS/MS with CH_3F gas in the CRC for direct Sr isotope analysis of glass-type geological RMs with high Rb/Sr ratios (0.02–0.67). The Q1 is set to the *m/z* ratio of the target mass (e.g., $^{87}Sr^+$, $^{85}Rb^+$or $^{87}Rb^+$), and the ions leaving the reaction cell are filtered by the Q2 set to the *m/z* ratio corresponding to either the primary reaction product (e.g., $^{87}Sr^{19}F^+$) or the unreacted ion (e.g., $^{85}Rb^+$or $^{87}Rb^+$). The external precision of $^{87}Sr/^{86}Sr$ isotope ratio was 0.05 ~ 0.3 %.

In situ Rb–Sr dating of Rb- and K-rich minerals (including biotite, muscovite, and K-feldspar) by LA–ICP–MS/MS was first achieved by Zack and Hogmalm (2016) at the University of Gothenburg, Sweden. Using O_2 as the reaction gas, part of the ablated Sr reacted to form SrO^+, whereas no RbO^+ was formed. The accuracy of the measured Rb–Sr isochron ages was better than 1.5 %, and that of the initial $^{87}Sr/^{86}Sr$ ratios was better than 0.2 %. Subsequently, Hogmalm et al. (2017) adopted two new reaction gases, N_2O and SF_6, which achieved higher reaction efficiencies than O_2. Nearly 100 % of the Sr reacted with N_2O to form SrO^+, and > 70 % of the Sr reacted with SF_6 to form SrF^+, while < 0.01 % of the Rb reacted with either gas. The sensitivity of SrO^+ and SrF^+ in obtaining Sr contents is 10 and 6 times higher, respectively, than that when using O_2 as the reaction gas. With these more reactive gases, the error in mica isochron ages is < 1 %. At present, N_2O is the most widely used reaction gas for LA Rb–Sr dating.

The effect of elemental fractionation and matrix effects on the accuracy and precision of Rb–Sr dating during LA–ICP–MS/MS analysis have been investigated. Gorojovsky and Aland (2020) used NIST 610 and BHVO-2G RMs and nano-powder phlogopite pellets (CRPG Mica-Mg-NP) RM to test the effects of laser wavelength (213 nm and 193 nm), laser frequency (5 Hz and 10 Hz), laser carrier gas (He, H_2, and N_2), dwell time, and external standard calibration on the accuracy and precision of $^{87}Rb/^{86}Sr$ and $^{87}Sr/^{86}Sr$ ratios. The results showed that the accuracy and precision of $^{87}Rb/^{86}Sr$ and $^{87}Sr/^{86}Sr$ ratios are significantly affected by laser wavelength and frequency. The best accuracy and precision were obtained when using a laser wavelength of 193 nm and ablating at a frequency of 5 Hz, which achieved internal precisions (2σ) of 0.3 % and 0.15 % for $^{87}Rb/^{86}Sr$ and $^{87}Sr/^{86}Sr$ ratios, respectively. For internal calibration, better accuracy is obtained with the addition of H_2 as a trace gas.

RMs play an important role in monitoring data quality and validating measurement procedures, and they are the most direct and effective method for correcting chemical and isotopic fractionation and matrix effects (Jochum and Nohl, 2008). At present, the commonly used RMs for *in situ* Rb-Sr dating include standard glasses (NIST SRM 610 and 612, USGS BCR-2 g and BHVO-2 g basaltic glasses) and phlogopite nano-powder pellets (CRPG Mica-Mg-NP; Zack and Hogmalm, 2016; Hogmalm et al., 2017; Şengün et al., 2019; Armistead et al., 2020; Gorojovsky and Alard, 2020; Li et al., 2020; Olierook et al., 2020; Tillberg et al., 2020; Redaa et al., 2021). Some MPI-Ding glass standards are also used as RMs for laser Rb–Sr dating, including ATHO-G (rhyolite), T1-G (quartz diorite), and StHs6/80-G (andesite; Laureijs et al., 2021). Redaa et al. (2022) and Jegal et al. (2022) assessed the chemical and isotopic compositions and homogeneity of phlogopite (Mica-Mg-NP), glauconite (GL-O-NP), biotite (Mica-Fe-NP), and K-feldspar (FK-N-NP) nano-powder pellets and fused glasses, and their suitability for *in situ*

Rb–Sr dating of K-rich silicate minerals using LA–ICP–MS/MS. The results showed that only the two nano-powders (Mica-Mg-NP and GL-O-NP) were suitable for *in situ* Rb–Sr dating by LA–ICP–MS/MS, given their homogeneity. However, Redaa et al. (2021) observed that Mica-Mg-NP and natural phlogopite have variable elemental fractionation and ablation characteristics, resulting in age deviations of ~ 7 % for natural phlogopite when using chemically consistent nano-powders as an external standard. This indicates that not only chemical properties but also physical properties can significantly magnify matrix effect. Therefore, developing mineral-specific, matrix-matched RMs for phlogopite and other Rb- and K-rich minerals is needed. Additional secondary mineral standards of known age are also required for more reliable Rb–Sr age determinations. Using a secondary mineral standard enables proper assessment of data quality and allows age offset corrections to be calculated (Armistead et al., 2020; Li et al., 2020). Huang et al (2023) proposed that GBW ZBH-25 biotite was a good secondary RM for *in situ* Rb-Sr dating.

LA–ICP–MS/MS Rb–Sr dating has been used to constrain the timing of tectono-thermal events in shear zones (Tillberg et al., 2020, 2021; Redaa et al., 2022; Liebmann et al., 2022; Wang et al., 2022; Ribeiro et al., 2023), Cu–Au and vein mineralization (Tillberg et al., 2017; Şengün et al., 2019; Olierook et al., 2020), tracing crustal evolution in cratons and orogens (Li et al., 2020; Gou et al., 2022) and the evolution of oceanic crust (Laureijs et al., 2021). Proterozoic marine sedimentary rocks dominated by shales have also been dated by analyzing paragenetic illite (Subarkah et al., 2021). Another field of application is the provenance of micas. Radiogenic Sr is hosted dominantly in micas, especially in old or highly differentiated sources; therefore, single-grain mica ages can be calculated from measured $^{87}Sr/^{87}Rb$ ratios if the initial $^{87}Sr/^{87}Rb$ ratio can be estimated. Rösel and Zack (2022) proposed a range of geologically relevant initial $^{87}Sr/^{87}Rb$ ratios, including 0.703 ± 0.003 for mantle derived magmatic rocks, 0.715 ± 0.015 for evolved magmatic rocks, and 0.730 ± 0.030 for crustal rocks. Using this method, hundreds of detrital mica grains can be analyzed per day.

3.2.3. Lu–Hf dating

The β-decay of ^{176}Lu produces ^{176}Hf, with a half-life of ~ 37.12 Gy (Scherer et al., 2001). Traditional applications of this method require time-consuming chemical separation of the parent (^{176}Lu) and daughter (^{176}Hf) isotopes, which is commonly accompanied by the loss of textural context of the analyzed minerals. Accurate *in situ* measurement of these isotopes is hindered by isobaric interferences from both ^{176}Lu and ^{176}Yb on ^{176}Hf.

With the Agilent 8800 ICP–MS/MS coupled to a LA system, Zack and Hogmalm (2015) explored the removal of the isobaric interference from ^{176}Lu and ^{176}Yb on ^{176}Hf. Approximately 50 % of the Hf is transmitted in mass-shift mode relative to that transmitted using no reaction gas, whereas < 0.05 % of the Lu and < 0.00005 % of the Yb are transmitted. This technique was used to date a 1.8 Ga old xenotime, which had high Lu/Hf (1000) and Yb/Hf (10000) ratios and yielded a Lu–Hf age that was within error of the U–Pb age and $^{176}Hf^*/^{176}Lu$ ratios of 0.0345 ± 1.4 % (2 s). Simpson et al. (2021) proposed a LA–ICP–MS/MS method using NH_3 as the cell gas and used this method to date garnet, apatite, and xenotime. The resulting uncertainties in the isochron ages were as low as ~ 0.5 % (95 % confidence interval). Similar LA–ICP–MS/MS methods using NIST 610 as a primary RM have been applied in Lu–Hf dating of calcite (Simpson et al., 2022), fluorite (Glorie et al., 2023), and phosphates (merrillite and stanfieldite in pallasite meteorites; Glorie et al., 2022). Although laser-based Lu–Hf dating has the advantage of being less prone to laser-induced isotopic fractionation than U–Pb, Wu et al. (2023) found matrix-induced bias (i.e., determined age/recommended age) between NIST 610 and xenotime, NIST 610 and apatite, and NIST 610 and garnet of 1.13–1.30, 1.148–1.151, and 1.049–1.051, respectively, indicating a significant matrix effect between NIST 610 glass and natural minerals. Hence, using secondary matrix-matched RMs for calibration of age bias and quality control during LA–ICP–MS/MS Lu–Hf dating is necessary to obtain meaningful ages.

In situ laser-based Lu–Hf, Sm–Nd, and U–Pb apatite dating has been used to study polymetamorphic histories within individual multi-growth garnets to reveal the thermo-tectonic history of the North Atlantic Craton (Simpson et al., 2023). The Lu–Hf and Sm–Nd isotopic systems in these apatites record a regional high-temperature metamorphic event at ~ 2.7 Ga, whereas the U–Pb system records a milder thermal event at ~ 1.7 Ga. This decoupling of the U–Pb system from the Sm–Nd and Lu–Hf systems reflects different closure temperatures. The higher closure temperatures of the Lu–Hf and Sm–Nd systems (>700 °C; Cherniak, 2000) prevented the re-equilibration of these systems during the milder event, whereas the diffusion of Pb at temperatures of < 450 °C at 1.7 Ga reset the U–Pb age, demonstrating that the Lu–Hf and Sm–Nd are more robust and thus more likely to faithfully record high temperature events than the U–Pb system.

A current limitation of *in situ* Lu–Hf dating is the large laser spot size (>120 μm) necessary to accurately measure Hf isotopic compositions; therefore, the sensitivity of the instrument and mass-shift efficiency of Hf should be enhanced in future. Isotopically homogenous primary RMs and secondary RMs with well-known ages should also be sought to further improve the accuracy and precision of ages.

3.2.4. Re–Os dating

^{187}Re decays to produce ^{187}Os by β-decay with a half-life of 42.3 Gy; it provides one of the few options for directly dating sulfide mineralization events. Molybdenite (MoS_2) is the most attractive target for Re–Os dating due to its high partition coefficient for Re and negligible common Os. Molybdenite Re–Os ages represent the crystallization age of molybdenite precipitated from hydrothermal fluids (Selby and Creaser, 2001). Dating of molybdenite is hindered by several analytical complications and is only performed in highly specialized labs. The main problem is that the different masses of ^{187}Re and ^{187}Os cannot be resolved by mass spectrometry, and chemical separation of these isotopes is difficult.

In situ Re–Os dating of molybdenite has been attempted using LA–ICP–MS/MS with methane (CH_4) in the CRC. Hogmalm et al. (2019) demonstrated that CH_4 reacted efficiently with Os^+ to form $OsCH_2^+$ (~70 % conversion), while 1 %–2% of the parent isotope Re also reacted to $ReCH_2$, leaving significant interference that was corrected mathematically. Six natural molybdenite samples from a range of geological settings with Re contents of > 10 ppm were analyzed using laser spots diameter of 70 μm, and ages were calibrated using molybdenite nanopowder pellets, yielding precise (1 %–5%; 2 s) and accurate (<1%, compared with ID-TIMS) ages.

Although LA–ICP–MS/MS does yield ages with external precision close to those of ID–TIMS in some cases, the effect of micro-scale parent-daughter decoupling on age accuracy is still controversial while using *in situ* method, such as NanoSIMS and LA-ICP-MS/MS. Previous work (Stein et al., 2003; Selby and Creaser, 2004) has shown that radiogenic ^{187}Os may not remain in the crystallographic site previously occupied by the parent, ^{187}Re, as it has a different ionic radius, bond length, and oxidation state. This means that the parent and daughter isotopes may become spatially decoupled with time, and the amount of daughter isotope collected when sampled is not directly proportional to the initial parent isotope content and the time elapsed. Zimmerman et al. (2022) obtained highly inaccurate molybdenite Re–Os ages relative to the ID–TIMS values, indicating that the measurement of ^{187}Os by LA–ICP–MS/MS is too imprecise to preclude parent–daughter decoupling to an extent that prevents high-precision geochronology. Sampling at the micron-scale (70–100 μm) may not overcome decoupling, thereby resulting in inaccurate radiometric ages. A full 2D or 3D LA–ICP–MS/MS scan and the homogenization of an entire crystal may yield more precise Re–Os ages.

Furthermore, sample heterogeneity can be mistaken for decoupling. A series of well-characterized, homogenous molybdenite RMs are required to correct for instrument fractionation and monitor data

quality.

4. Future applications in metallogeny

Chemical data on a greater range of natural ore and hydrothermal minerals would be invaluable in understanding the fundamental controls on trace-element distribution and interpreting the conditions of ore formation in a variety of settings (Cook et al., 2016). LA-ICP–MS/MS offers many advantages to expend this to minerals for which little or no LA–ICP–MS trace-element data are currently available, including REEs in Sn-rich minerals (such as cassiterite and stannite), Ba-rich minerals (witherite, barite), bonamite and molybdenite; noble metals in Cu-Fe-Zn-Ni sulfides, REE-rich minerals, W-rich minerals (such as wolframite and scheelite) and columbo-tantalite minerals; halogens in hydrothermal minerals (such as apatite, micas, amphibole, etc). Considerable opportunity also exists for LA–ICP–MS/MS studies addressing the partitioning of potential economic metals, including Sc, Sb and Ge, in multiphase sulfide–oxide–silicate assemblages. Such additional data will assist in building element distribution models and assessing the source of metals and fluids.

In addition, ICP–MS/MS provides an unprecedented laser-based method for *in situ* dating using β-decay systems (including ^{87}Rb–^{87}Sr, ^{176}Lu–^{176}Hf, ^{187}Re–^{187}Os, ^{138}La–^{138}Ce, and ^{40}K–^{40}Ca) in common ore and gangue minerals. The datable minerals, methods, and applicable deposit types are listed in Table 5. The closure temperatures of the Rb–Sr system in K-bearing minerals (e.g., K-feldspar = 200–300 °C; biotite = 300–400 °C; mica = 500–550 °C; phlogopite = 400–600 °C; amphibole = 450–550 °C; Armstrong et al., 1966; Verschure et al., 1980; Blanckenburg et al., 1989; Willigers et al., 2004) cover the range of common temperatures of hydrothermal alteration and mineralization (200–600 °C; Sillitoe, 2010); therefore, direct analysis of the Rb–Sr isotopic compositions of hydrothermal K-rich minerals can provide age information for hydrothermal alteration and mineralization. Several recent publications have explored *in situ* Rb–Sr dating of muscovite and biotite to better understand the genesis of orogenic Au deposits (Şengün et al., 2019; Olierook et al., 2020) and vein mineralization (Tillberg et al., 2017). Additionally, LA-ICP-MS/MS has great potential for *in situ* dating of Rb-rich ore minerals (such as amazonite, lepidolite, pollucite with Rb_2O content up to 3.3 %) in Li-, Rb-and Cs-rare metal deposits. Although LA-ICP-MS/MS is powerful, the application of *in situ* Rb-Sr dating is still limited due to the precision and accumulation of radiogenic ^{87}Sr. So, only limited minerals with high Rb/Sr ratios could be used for *in situ* Rb-Sr dating.

Another large field of potential applications is directly dating HREE-rich minerals, including xenotime, euxenite, gadolinite, and apatite, using *in situ* Lu–Hf LA–ICP–MS/MS dating. These minerals can occur as the major ore minerals in HREE deposits. The Lu–Hf isotopic system in apatite generally has a higher closure temperature (>700 °C; Cherniak, 2000) than the U–Pb system (<450 °C); therefore, the Lu–Hf system is more robust and more likely to faithfully record high-temperature events than the U–Pb system and is promising for dating mafic magma-related deposits (Kharkongor et al., 2023). Furthermore, the several orders of magnitude improvement in abundance sensitivities attainable with MS/MS increases the potential for *in situ* Hf isotope analyses in samples with high-Ta and -W matrices, as the tail of the ^{180}Ta signal would affect the accurate determination of ^{179}Hf in single quadrupole mass spectrometry.

Future technical developments are likely to lead to smaller spot sizes and better spatial resolutions, in turn facilitating insights into finely zoned or intergrown minerals that cannot be analyzed at present. Maximizing the sensitivity of ICP–MS/MS is expected with future study. There has also been increasing interest in *in situ* dating of β-decay systems using LA coupled with CRC–MC–ICP–MS instruments (Bevan et al., 2021; Craig et al., 2021; Dauphas et al., 2022), which can improve the precision and external reproducibility relative to that of quadrupole based ICP–MS/MS, leading to the hope that minerals with relatively low contents and with requirement of high analytical precision (such as ^{138}La–^{138}Ce, and ^{40}K–^{40}Ca) can be accurately dated using *in situ* LA technique. A novel single-spot Rb–Sr isochron method for dating biotite has been developed using CRC–MC–ICP–MS (Cruz-Uribe et al., 2023). This technique allows sub-spot Rb–Sr dating within individual laser spots, obtaining multiple dates within a single time-resolved analysis, leading to potential applications in revealing multiple heating, cooling, and fluid-alteration events within small domains in single biotite crystals. This technique is expected to be expanded to include other β-decay systems. Another limitation of MS/MS based dating is a lack of well-characterized matrix matched RMs. Currently, the largest source of uncertainty comes from the matrix effect arising from the different ablation behaviors of different materials (Zack and Hogmalm, 2016). Developing more reliable matrix-matched RMs is needed.

In conclusion, the advances in LA–ICP–MS/MS described in this review are having a profound effect on geochemistry and *in situ* β-decay geochronology in studies of mineral deposits. ICP–MS/MS technology was introduced onto the market only ten years ago, but since then new applications have frequently been described. It may, therefore, be assumed that over the next few years, (LA)–ICP–MS/MS will grow

Table 5
Datable minerals by LA–ICP–MS/MS using β-decay systems and applicable deposit types.

Minerals	Datable method	Mass fractions (Mean ± SD, μg/g)	External precision (%) (3)	Applicable deposit type
Ore minerals				
Molybdenite (1)	Re–Os	Re: 248 ± 349; Os: 1.4 ± 3.0	~1–5 %	Porphyry Cu–Au, VMS Cu–Pb–Zn, epithermal Au
Hydrothermal minerals				
Biotite (1)	Rb–Sr	Rb: 676 ± 1082; Sr: 24 ± 98	~1–3 %	Porphyry Cu–Au
Muscovite, sericite (1)	Rb–Sr	Rb: 1564 ± 1423; Sr: 34 ± 308	~1–3 %	Epithermal Au, orogenic Au, porphyry Cu–Au, VMS Cu–Pb–Zn
K-feldspar (orthoclase, adularia) (1)	Rb–Sr	Rb: 316 ± 1334; Sr: 398 ± 1082	~1–5 %	Porphyry Cu–Au, epithermal Au
Clay minerals (illite, smectite) (1)	Rb–Sr	Rb: 26 ± 45; Sr: 218 ± 236	~1–5 %	Epithermal Au, Carlin Au, orogenic Au, MVT Pb–Zn, VMS Cu–Pb–Zn
Amazonite, lepidolite, pollucite	Rb–Sr	Rb_2O: 1.4 % ~3.3 %	n.a.	Li-, Rb-and Cs-rare metal deposit
Fluorite (2)	Lu–-Hf	Lu: ~0.03–4	~1–20 %	MVT Pb–Zn, pegmatite polymetals
Garnet (1)	Lu–Hf	Lu: 2 ± 12; Hf: 5 ± 38; U: 4 ± 18; Pb: 3 ± 36	~1–3 %	Skarn Cu-Au
Apatite (1)	Lu–Hf	Lu: 11 ± 88; Hf: 1 ± 16; U: 23 ± 157; Pb: 34 ± 800	~1–3 %	Porphyry Cu–Au, mafic magma related deposits, rare-earth deposit
Calcite (1)	Lu–Hf	Lu: 3 ± 31; Hf: 3 ± 30; U: 21 ± 50; Pb: 5 ± 70	~1–5 %	epithermal Au, orogenic Au

(1) Mean mass fractions are calculated based on data from the GEOROC database (https://georoc.eu/) accessed on 25 July 2023.
(2) Glorie et al. (2023).
(3) The external precision is calculated simply based on age and error values published in previous articles and is largely dependent on the Re, Rb, and Lu mass fractions.

exponentially in use, as it provides a powerful complement to the shortcomings of single-quadrupole ICP–MS—and even sector-field ICP–MS in some cases—for many applications where ultra-trace elements have to be determined in complex matrices and where β-decay systems have to be dated within individual, *in situ* crystals.

Declaration of Competing Interest

The authors declare that they have no known competing financial interests or personal relationships that could have appeared to influence the work reported in this paper.

Data availability

Data will be made available on request.

Acknowledgments

This work was funded by the National Natural Science Foundation of China (41825005, 91955207) and Basic Research Foundation of Chinese Academy of Geological Sciences (JKYQN202317). The authors thank two anonymous reviewers for their constructive feedback during the manuscript review process, which helped to improve the manuscript, and thank Huayong Chen editor-in-chief for handling our manuscript.

References

Amr, M.A., Dawood, N.D.A., Helal, A.I., Russell, B., 2017. Rare earth elements and Nd-143/Nd-144 isotope ratio measurements using tandem ICP-CRC-MS/MS: characterization of date palm (Phoenix dactylifera L.). J. Anal. at. Spectrom. 32, 1554–1565. https://doi.org/10.1039/c7ja00126f.

Armentrout, P.B., Halle, L.F., Beauchamp, J.L., 1982. Reaction of chromium(1+), manganese(1+), iron(1+), cobalt(1+), and nickel(1+) ions with diatomic oxygen and nitrous oxide. Examination of the translational energy dependence of the cross sections of endothermic reactions. J. Chem. Phys. 76, 2449–2457. https://doi.org/10.1063/1.443274.

Armistead, S.E., Collins, A.S., Redaa, A., Jepson, G., Gillespie, J., Gilbert, S., Blades, M.L., Foden, J.D., Razakamanana, T., 2020. Structural evolution and medium-temperature thermochronology of Central Madagascar: implications for Gondwana amalgamation. J. Geol. Soc. 177, 784–798. https://doi.org/10.1144/jgs2019-132.

Armstrong, R.L., Jäger, E., Eberhardt, P., 1966. A comparison of K-Ar and Rb-Sr ages on Alpine biotites. Earth Planet. Sci. Lett. 1, 13–19.

Balcaen, L., Woods, G., Resano, M., Vanhaecke, F., 2013. Accurate determination of S in organic matrices using isotope dilution ICP-MS/MS. J. Anal. at. Spectrom. 28, 33–39. https://doi.org/10.1039/c2ja30265a.

Balaram, V., 2021. Strategies to overcome interferences in elemental and isotopic geochemical analysis by quadrupole inductively coupled plasma mass spectrometry: A critical evaluation of the recent developments. Rapid Commun. Mass Spectrom. 35, e9065. https://doi.org/10.1002/rcm.9065.

Balcaen, L., Bolea-Fernandez, E., Resano, M., Vanhaecke, F., 2015. Inductively coupled plasma-Tandem mass spectrometry (ICP-MS/MS): A powerful and universal tool for the interference-free determination of (ultra)trace elements-A tutorial review. Anal. Chim. Acta. 894, 7–19. https://doi.org/10.1016/j.aca.2015.08.053.

Balcone-Boissard, H., 2009. Simultaneous determination of fluorine, chlorine, bromine and iodine in six geochemical reference materials using pyrohydrolysis, ion chromatography and inductively coupled plasma-mass spectrometry. Geostand. Geoanal. Res. 33, 477–485. https://doi.org/10.1111/j.1751-908X.2009.00018.x.

Barefoot, R.R., 2004. Determination of platinum group elements and gold in geological materials: a review of recent magnetic sector and laser ablation applications. Anal. Chim. Acta. 509, 119–125. https://doi.org/10.1016/j.aca.2003.12.031.

Becker, J.S., 2005. Inductively coupled plasma mass spectrometry (ICP-MS) and laser ablation ICP-MS for isotope analysis of long-lived radionuclides. Int. J. Mass Spectrom. 242, 183–195. https://doi.org/10.1016/j.ijms.2004.11.009.

Bencs, L., Ravindra, K., Van Grieken, R., 2003. Methods for the determination of platinum group elements originating from the abrasion of automotive catalytic converters. Spectrochim. Acta B At. Spectrosc. 58, 1723–1755. https://doi.org/10.1016/s0584-8547(03)00162-9.

Bevan, D., Coath, C.D., Lewis, J., Schwieters, J., Lloyd, N., Craig, G., Wehrs, H., Elliott, T., 2021. In situ Rb-Sr dating by collision cell, multicollection inductively-coupled plasma mass-spectrometry with pre-cell mass-filter, (CC-MC-ICPMS/MS). J. Anal. at. Spectrom. 36, 917–931. https://doi.org/10.1039/d1ja00006c.

Bi, X.W., Cornell, D.H., Hu, R.Z., 2002. REE composition of primary and altered feldspar from the mineralized alteration zone of alkaline intrusive rocks, western Yunnan Province China. Ore Geol. Rev. 19, 69–78.

Bierlein, F.P., 1995. Rare-earth element geochemistry of elastic and chemical metasedimentary rocks associated with hydrothermal sulfide mineralization in the Olary Block, South Australia. Chem. Geol. 122, 77–98. https://doi.org/10.1016/0009-2541(94)00152-X.

Blanckenburg, F., Villa, I.M., Baur, H., Morteani, G., Steiger, R.H., 1989. Time calibration of a PT-path from the Western Tauern Window, Eastern Alps: the problem of closure temperatures. Contrib. Mineral. Petrol. 101, 1–11.

Bolea-Fernandez, E., Balcaen, L., Resano, M., Vanhaecke, F., 2014. Potential of methyl fluoride as a universal reaction gas to overcome spectral interference in the determination of ultratrace concentrations of metals in biofluids using inductively coupled plasma-tandem mass spectrometry. Anal. Chem. 86, 7969–7977. https://doi.org/10.1021/ac502023h.

Bolea-Fernandez, E., Van Malderen, S.J.M., Balcaen, L., Resano, M., Vanhaecke, F., 2016. Laser ablation-tandem ICP-mass spectrometry (LA-ICP- MS/MS) for direct Sr isotopic analysis of solid samples with high Rb/Sr ratios. J. Anal. at. Spectrom. 31, 464–472. https://doi.org/10.1039/c5ja00404g.

Bolea-Fernandez, E., Balcaen, L., Resano, M., Vanhaecke, F., 2017. Overcoming spectral overlap via inductively coupled plasma-tandem mass spectrometry (ICPMS/MS). A tutorial review. J. Anal. at. Spectrom. 32, 1660–1679. https://doi.org/10.1039/c7ja00010c.

Bolea-Fernandez, E., Rua-Ibarz, A., Resano, M., Vanhaecke, F., 2021. To shift, or not to shift: adequate selection of an internal standard in mass-shift approaches using tandem ICP-mass spectrometry (ICP-MS/MS). J. Anal. at. Spectrom. 36, 1135–1149. https://doi.org/10.1039/d0ja00438c.

Boulyga, S.F., Becker, J.S., 2002. Improvement of abundance sensitivity in a quadrupole-based ICP-MS instrument with a hexapole collision cell. J. Anal. at. Spectrom. 17, 1202–1206. https://doi.org/10.1039/b203086c.

Brenner, I.B., Taylor, H.E., 1992. A critical-review of inductively coupled plasma-mass spectrometry for geoanalysis, geochemistry, and hydrology. Part I. Analytical Performance. Crit. Rev. Anal. Chem. 23, 355–367. https://doi.org/10.1080/10408349208051650.

Cao, K., Yang, Z.-M., Hou, Z.-Q., White, N.C., Yu, C., 2021. Contrasting porphyry Cu fertilities in the Yidun Arc, Eastern Tibet: Insights from zircon and apatite compositions and implications for exploration. In SEG Special Publication 231–255.

Cherniak, D.J., 2000. Rare earth element diffusion in apatite. Geochim. Cosmochim. Acta 64, 3871–3885. https://doi.org/10.1016/S0016-7037(00)00467-1.

Chew, D.M., Petrus, J.A., Kamber, B.S., 2014. U-Pb LA–ICPMS dating using accessory mineral standards with variable common Pb. Chem. Geol. 363, 185–199. https://doi.org/10.1016/j.chemgeo.2013.11.006.

Chiaradia, M., Schaltegger, U., Spikings, R., 2014. Time scales of mineral systems—advances in understanding over the past decade. SEG Special Publications. 18, 37–58.

Cook, N., Ciobanu, C.L., George, L., Zhu, Z.-Y., Wade, B., Ehrig, K., 2016. Trace element analysis of minerals in magmatic-hydrothermal rres by laser ablation inductively-coupled plasma mass spectrometry: approaches and opportunities. Minerals. 6 https://doi.org/10.3390/min6040111.

Cooke, D.R., Agnew, P., Hollings, P., Baker, M., Chang, Z., Wilkinson, J.J., Ahmed, A., White, N.C., Zhang, L., Thompson, J., Gemmell, J.B., Danyushevsky, L., Chen, H., 2020. Recent advances in the application of mineral chemistry to exploration for porphyry copper-gold-molybdenum deposits: detecting the geochemical fingerprints and footprints of hypogene mineralization and alteration. Geochem.: Explor. Environ. Anal. 20, 176–188. https://doi.org/10.1144/geochem2019-039.

Cruz-Uribe, A. M., Craig, G., Garber, J. M., Paul, B., Arkula, C., and Bouman, C. 2023. Single spot Rb-Sr isochron dating of biotite by LA-MC-ICP-MS/MS. Geostand. Geoanal. Res., https://doi.org/10.1111/ggr.12518.

Dams, R.F.J., Goossens, J., Moens, L., 1995. Spectral and non-spectral interferences in inductively-coupled plasma mass-spectrometry. Mikrochim. Acta. 119, 277–286. https://doi.org/10.1007/BF01244007.

Dauphas, N., Hopp, T., Craig, G., Zhang, Z.J., Valdes, M.C., Heck, P.R., Charlier, B.L.A., Bell, E.A., Harrison, T.M., Davis, A.M., Dussubieux, L., Williams, P.R., Krawczynski, M.J., Bouman, C., Lloyd, N.S., Tollstrup, D., Schwieters, J.B., 2022. In situ 87Rb–87Sr analyses of terrestrial and extraterrestrial samples by LA-MC-ICP-MS/MS with double Wien filter and collision cell technologies. J. Anal. at. Spectrom. 37, 2420–2441. https://doi.org/10.1039/d2ja00135g.

Diez Fernández, S., Ruiz Encinar, J., Sanz-Medel, A., Isensee, K., Stoll, H.M., 2015. Determination of low B/Ca ratios in carbonates using ICP-QQQ. Geochem. Geophysics, Geosys. 16, 2005–2014. https://doi.org/10.1002/2015gc005817.

Diez-Fernandez, S., Isnard, H., Nonell, A., Bresson, C., Chartier, F., 2020. Radionuclide analysis using collision-reaction cell ICP-MS technology: a review. J. Anal. at. Spectrom. 35, 2793–2819. https://doi.org/10.1039/d0ja00211a.

Ding, X., Bu, W., Ni, Y., Shao, X., Xiong, K., Yang, C., Hu, S., 2021. Determination of trace rare earth elements in uranium ore samples by triple quadrupole inductively coupled plasma mass spectrometry. J. Anal. at. Spectrom. 36, 2144–2152. https://doi.org/10.1039/d1ja00218j.

Economou-Eliopoulos, M., 1996. Platinum-group element distribution in chromite ores from ophiolite complexes: Implications for their exploration. Ore Geol. Rev. 11, 363–381. https://doi.org/10.1016/S0169-1368(96)00008-X.

Feldmann, I., Jakubowski, N., Stuewer, D., 1999a. Application of a hexapole collision and reaction cell in ICP-MS Part I: Instrumental aspects and operational optimization. Fresen. J. Anal. Chem. 365, 415–421. https://doi.org/10.1007/s002160051633.

Feldmann, I., Jakubowski, N., Thomas, C., Stuewer, D., 1999b. Application of a hexapole collision and reaction cell in ICP-MS Part II: Analytical figures of merit and first applications. Fresen. J. Anal. Chem. 365, 422–428. https://doi.org/10.1007/s002160051634.

Fletcher, N.D., Manard, B.T., Metzger, S.C., Ticknor, B.W., Bostick, D.A., Hexel, C.R., 2020. Determining P, S, Br, and I content in uranium by triple quadrupole inductively coupled plasma mass spectrometry. J. Radioanal. Nucl. Chem. 324, 395–402. https://doi.org/10.1007/s10967-020-07057-0.

Gilbert, S.E., Glorie, S., 2020. Removal of Hg interferences for common Pb correction when dating apatite and titanite by LA-ICP-MS/MS. J. Anal. at. Spectrom. 35, 1472–1481. https://doi.org/10.1039/d0ja00224k.
Gillespie, J., Kirkland, C.L., Kinny, P.D., Simpson, A., Glorie, S., Rankenburg, K., 2022. Lu–Hf, Sm–Nd, and U-Pb isotopic coupling and decoupling in apatite. Geochim. Cosmochim. Acta 338, 121–135. https://doi.org/10.1016/j.gca.2022.09.038.
Glorie, S., Burke, T., Hand, M., Simpson, A., Gilbert, S., Wade, B., 2022. In situ Lu-Hf phosphate geochronology: progress towards a new tool for space exploration. Geosci. Front. 13 https://doi.org/10.1016/j.gsf.2022.101375.
Glorie, S., Mulder, J., Hand, M., Fabris, A., Simpson, A., Gilbert, S., 2023. Laser ablation (in situ) Lu-Hf dating of magmatic fluorite and hydrothermal fluorite-bearing veins. Geosci. Front. https://doi.org/10.1016/j.gsf.2023.101629.
Gorojovsky, L., Alard, O., 2020. Optimisation of laser and mass spectrometer parameters for the in situ analysis of Rb/Sr ratios by LA-ICP-MS/MS. J. Anal. at. Spectrom. 35, 2322–2336. https://doi.org/10.1039/d0ja00308e.
Gou, L.-L., Long, X.-P., Yan, H.-Y., Shu, T.-C., Wang, J.-Y., Xu, X.-F., Zhou, F., Tian, Z.-B., 2022. Metamorphic P-T evolution and in situ biotite Rb–Sr geochronology of garnet–staurolite schist from the Ramba gneiss dome in the Northern Himalaya. Front. Earth Sci. 10, 887154 https://doi.org/10.3389/feart.2022.887154.
Groves, D.I., Goldfarb, R.J., Gebre-Mariam, M., Hagemann, S.G., Robert, F., 1998. Orogenic gold deposits: A proposed classification in the context of their crustal distribution and relationship to other gold deposit types. Ore Geol. Rev. 13, 7–27. https://doi.org/10.1016/S0169-1368(97)00012-7.
Guo, W., Jin, L., Hu, S., Guo, Q., 2017. Method development for the determination of total fluorine in foods by tandem inductively coupled plasma mass spectrometry with a mass-shift strategy. J. Agric. Food Chem. 65, 3406–3412. https://doi.org/10.1021/acs.jafc.7b00535.
Harouaka, K., Allen, C., Bylaska, E., Cox, R.M., Eiden, G.C., di Vacri, M.L., Hoppe, E.W., Arnquist, I.J., 2021. Gas-phase ion-molecule interactions in a collision reaction cell with triple quadrupole-inductively coupled plasma mass spectrometry: Investigations with N2O as the reaction gas. Spectrochim. Acta - Part B at. Spectroscopy. 186 https://doi.org/10.1016/j.sab.2021.106309.
Harouaka, K., Melby, K., Bylaska, E.J., Cox, R.M., Eiden, G.C., French, A., Hoppe, E.W., Arnquist, I.J., 2022. Gas-phase ion-molecule interactions in a collision reaction cell with ICP-MS/MS: investigations with CO2 as the reaction gas. Geostand. Geoanal. Res. 46, 387–399. https://doi.org/10.1111/ggr.12429.
Hawkes, H.E., Webb, J.S., 1962. Geochemistry in mineral exploration. Harper and Row, New York, p. 415.
Hedenquist, J.W., Lowenstern, J.B., 1994. The role of magmas in the formation of hydrothermal ore-deposits. Nature 370, 519–527. https://doi.org/10.1038/370519a0.
Hogmalm, K.J., Zack, T., Karlsson, A.K.O., Sjöqvist, A.S.L., Garbe-Schönberg, D., 2017. In situ Rb–Sr and K-Ca dating by LA-ICP-MS/MS: an evaluation of N2O and SF6 as reaction gases. J. Anal. at. Spectrom. 32, 305–313. https://doi.org/10.1039/c6ja00362a.
Hogmalm, K.J., Dahlgren, I., Fridolfsson, I., Zack, T., 2019. First in situ Re-Os dating of molybdenite by LA-ICP-MS/MS. Miner. Deposita 54, 821–828. https://doi.org/10.1007/s00126-019-00889-1.
Huang, C., Wang, H., Shi, W., Sun, J., Hu, F., Xu, L., Yang, Y., Wu, S., Xie, L., Yang, J., 2023. In situ Rb-Sr dating of mica by LA-ICP-MS/MS. Sci. China Earth Sci. https://doi.org/10.1007/s11430-022-1138-4.
Ismail, S.A., Kettanah, Y.A., Chalabi, S.N., Ahmed, A.H., Arai, S., 2014. Petrogenesis and PGE distribution in the Al- and Cr-rich chromitites of the Qalander ophiolite, northeastern Iraq: Implications for the tectonic environment of the Iraqi Zagros Suture Zone. Lithos 202, 21–36. https://doi.org/10.1016/j.lithos.2014.05.013.
Jamari, N. L. A., Dohmann, J. F., Raab, A., Krupp, E. M., Feldmann, J. Novel non-target analysis of fluorine compounds using ICPMS/MS and HPLC-ICPMS/MS. J. Anal. At. Spectrom. 32, 942-950. https://doi.org/10.1039/c7ja00051k.
Jegal, Y., Zimmermann, C., Reisberg, L., Yeghicheyan, D., Cloquet, C., Peiffert, C., Gerardin, M., Deloule, E., Mercadier, J., 2022. Characterisation of reference materials for in situ Rb-Sr dating by LA-ICP-MS/MS. Geostand. Geoanal. Res. 46, 645–671. https://doi.org/10.1111/ggr.12456.
Jochum, K.P., Nohl, U., 2008. Reference materials in geochemistry and environmental research and the GeoReM database. Chem. Geol. 253, 50–53. https://doi.org/10.1016/j.chemgeo.2008.04.002.
Kasapoğlu, B., Ersoy, Y.E., Uysal, İ., Palmer, M.R., Zack, T., Koralay, E.O., Karlsson, A., 2016. The petrology of Paleogene volcanism in the Central Sakarya, Nallıhan Region: implications for the initiation and evolution of post-collisional, slab break-off-related magmatic activity. Lithos 246–247, 81–98. https://doi.org/10.1016/j.lithos.2015.12.024.
Kelley, D.L., Benn, C., Riedell, K.B., Johnson, T., 2010. The role of geochemistry in Andean copper discoveries. SEG Special Publications. 15, 271–286.
Kharkongor, M.B.K., Glorie, S., Mulder, J., Kirkland, C.L., Chew, D., Kohn, B., Simpson, A., 2023. Apatite laser ablation Lu Hf geochronology: a new tool to date mafic rocks. Chem. Geol. 636 https://doi.org/10.1016/j.chemgeo.2023.121630.
Klein, O., Zimmermann, T., Pröfrock, D., 2021. Improved determination of technologically critical elements in sediment digests by ICP-MS/MS using N2O as a reaction gas. J. Anal. at. Spectrom. 36, 1524–1532. https://doi.org/10.1039/d1ja00088h.
Kutscher, D., Ducos, S.M., Nelms, S., Leykin, A., 2018. ICP-MS analysis of noble metals at low levels in geological reference materials and ores. Spectroscopy 33, 16–25.
Laureijs, C.T., Coogan, L.A., Spence, J., 2021. In-situ Rb-Sr dating of celadonite from altered upper oceanic crust using laser ablation ICP-MS/MS. Chem. Geol. 579 https://doi.org/10.1016/j.chemgeo.2021.120339.
Layton-Matthews, D., McClenaghan, M.B., 2022. Current techniques and applications of mineral chemistry to mineral exploration; examples from glaciated terrain: a review. Minerals. 12 https://doi.org/10.3390/min12010059.
Li, S.-S., Santosh, M., Farkaš, J., Redaa, A., Ganguly, S., Kim, S.W., Zhang, C., Gilbert, S., Zack, T., 2020. Coupled U-Pb and Rb-Sr laser ablation geochronology trace Archean to Proterozoic crustal evolution in the Dharwar Craton India. Precam. Res. 343 https://doi.org/10.1016/j.precamres.2020.105709.
Liebmann, J., Kirkland, C.L., Kelsey, D.E., Korhonen, F.J., Rankenburg, K., 2022. Lithological fabric as a proxy for Rb–Sr isotopic complexity. Chem. Geol. 608 https://doi.org/10.1016/j.chemgeo.2022.121041.
Liu, X., Dong, S., Yue, Y., Guan, Q., Sun, Y., Chen, S., Zhang, J., Yang, Y., 2020. (87) Sr/(86) Sr isotope ratios in rocks determined using inductively coupled plasma tandem mass spectrometry in O(2) mode without prior Sr purification. Rapid Commun. Mass Spectrom. 34, e8690.
Liu, Y., Hu, Z., Li, M., Gao, S., 2013. Applications of LA-ICP-MS in the elemental analyses of geological samples. Chinese Sci. Bull. 58, 3863–3878. https://doi.org/10.1007/s11434-013-5901-4.
Lum, T.-S., Leung, K.-S.-Y., 2016. Strategies to overcome spectral interference in ICP-MS detection. J. Anal. at. Spectrom. 31, 1078–1088. https://doi.org/10.1039/c5ja00497g.
Mitra, A., Sen, I.S., Walkner, C., Meisel, T.C., 2021. Simultaneous determination of platinum group elements and rhenium mass fractions in road dust samples using isotope dilution inductively coupled plasma-tandem mass spectrometry after cation exchange separation. Spectrochimica Acta - Part B Atom. Spec. 177 https://doi.org/10.1016/j.sab.2020.106052.
Moens, L.J., Vanhaecke, F.F., Bandura, D.R., Baranov, V.I., Tanner, S.D., 2001. Elimination of isobaric interferences in ICP-MS, using ion–molecule reaction chemistry: Rb/Sr age determination of magmatic rocks, a case study. J. Anal. at. Spectrom. 16, 991–994. https://doi.org/10.1039/b103707m.
O'Brien, J.J., Spry, P.G., Teale, G.S., Jackson, S.E., Rogers, D., 2015. Major and trace element chemistry of gahnite as an exploration guide to Broken Hill-Type Pb-Zn-Ag mineralization in the Broken Hill Domain, New South Wales Australia. Econ. Geol. 110, 1027–1057. https://doi.org/10.2113/econgeo.110.4.1027.
Olierook, H.K.H., Rankenburg, K., Ulrich, S., Kirkland, C.L., Evans, N.J., Brown, S., McInnes, B.I.A., Prent, A., Gillespie, J., McDonald, B., Darragh, M., 2020. Resolving multiple geological events using in situ Rb–Sr geochronology: implications for metallogenesis at Tropicana, Western Australia. Geochronology. 2, 283–303. https://doi.org/10.5194/gchron-2-283-2020.
Petrus, J.A., Kamber, B.S., 2012. VizualAge: a novel approach to laser ablation ICP-MS U-Pb geochronology data reduction. Geostand. Geoanal. Res. 36, 247–270. https://doi.org/10.1111/j.1751-908X.2012.00158.x.
Phillips, M.J.M., Foley, S.F., Alard, O., 2023. Application of Ge/Si ratios to ultramafic alkaline rocks using a novel LA-ICP- MS/MS method. Chem. Geol. 616 https://doi.org/10.1016/j.chemgeo.2022.121236.
Redaa, A., Farkaš, J., Gilbert, S., Collins, A.S., Wade, B., Löhr, S., Zack, T., Garbe-Schönberg, D., 2021. Assessment of elemental fractionation and matrix effects during in situ Rb–Sr dating of phlogopite by LA-ICP-MS/MS: implications for the accuracy and precision of mineral ages. J. Anal. At. Spectrom 36, 322–344. https://doi.org/10.1039/d0ja00299b.
Redaa, A., Farkaš, J., Gilbert, S., Collins, A.S., Löhr, S., Vasegh, D., Forster, M., Blades, M., Zack, T., Giuliani, A., Maas, R., Baldermann, A., Dietzel, M., Garbe-Schönberg, D., 2022a. Testing nano-powder and fused-glass mineral reference materials for in situ Rb-Sr dating of glauconite, phlogopite, biotite and feldspar via LA-ICP-MS/MS. Geostand. Geoanal. Res. 47, 23–48. https://doi.org/10.1111/ggr.12467.
Redaa, A., Farkaš, J., Hassan, A., Collins, A.S., Gilbert, S., Löhr, S.C., 2022b. Constraints from in-situ Rb-Sr dating on the timing of tectono-thermal events in the Umm Farwah shear zone and associated Cu-Au mineralisation in the Southern Arabian Shield Saudi Arabia. J. Asian Earth Sci. 224 https://doi.org/10.1016/j.jseaes.2021.105037.
Ribeiro, B.V., Kirkland, C.L., Kelsey, D.E., Reddy, S.M., Hartnady, M.I.H., Faleiros, F.M., Rankenburg, K., Liebmann, J., Korhonen, F.J., Clark, C., 2023. Time-strain evolution of shear zones from petrographically constrained Rb–Sr muscovite analysis. Earth Planet. Sci. Lett. 602 https://doi.org/10.1016/j.epsl.2022.117969.
Richards, J.P., 2003. Tectono-magmatic precursors for porphyry Cu-(Mo-Au) deposit formation. Econ. Geol. 98, 1515–1533. https://doi.org/10.2113/98.8.1515.
Rieger, P., Magnall, J.M., Gleeson, S.A., Oelze, M., Wilke, F.D.H., Lilly, R., 2022. Differentiating between hydrothermal and diagenetic carbonate using rare earth element and yttrium (REE plus Y) geochemistry: a case study from the Paleoproterozoic George Fisher massive sulfide Zn deposit, Mount Isa Australia. Mineralium Deposita. 57, 187–206. https://doi.org/10.1007/s00126-021-01056-1.
Rösel, D., and Zack, T. 2022. LA-ICP-MS/MS single-spot Rb-Sr dating. Geostand. Geoanal. Res., https://doi.org/10.1111/ggr.12414.
Scherer, E., Munker, C., Mezger, K., 2001. Calibration of the lutetium-hafnium clock. Science 293, 683–687. https://doi.org/10.1126/science.1061372.
Selby, D., Creaser, R.A., 2001. Re-Os geochronology and systematics in molybdenite from the Endako porphyry molybdenum deposit, British Columbia Canada. Econ. Geol. 96, 197–204.
Selby, D., Creaser, R.A., 2004. Macroscale NTIMS and microscale LA-MC-ICP-MS Re-Os isotopic analysis of molybdenite: Testing spatial restrictions for reliable Re-Os age determinations, and implications for the decoupling of Re and Os within molybdenite. Geochim. Cosmochim. Acta 68, 3897–3908. https://doi.org/10.1016/j.gca.2004.03.022.
Şengün, F., Bertrandsson Erlandsson, V., Hogmalm, J., Zack, T., 2019. In situ Rb-Sr dating of K-bearing minerals from the orogenic Akçaabat gold deposit in the

Menderes Massif, Western Anatolia Turkey. J. Asian Earth Sci. 185 https://doi.org/10.1016/j.jseaes.2019.104048.
Sillitoe, R.H., 2010. Porphyry copper systems. Econ. Geol. 105, 3–41. https://doi.org/10.2113/gsecongeo.105.1.3.
Simpson, A., Gilbert, S., Tamblyn, R., Hand, M., Spandler, C., Gillespie, J., Nixon, A., Glorie, S., 2021. In-situ Lu-Hf geochronology of garnet, apatite and xenotime by LA ICP MS/MS. Chem. Geol. 577 https://doi.org/10.1016/j.chemgeo.2021.120299.
Simpson, A., Glorie, S., Hand, M., Spandler, C., Gilbert, S., Cave, B., 2022. In situ Lu–Hf geochronology of calcite. Geochronology. 4, 353–372. https://doi.org/10.5194/gchron-4-353-2022.
Simpson, A., Glorie, S., Hand, M., Spandler, C., Gilbert, S., 2023. Garnet Lu-Hf speed dating: a novel method to rapidly resolve polymetamorphic histories. Gondw. Res. 121, 215–234. https://doi.org/10.1016/j.gr.2023.04.011.
Song, S., Mao, J., Xie, G., Chen, L., Santosh, M., Chen, G., Rao, J., Ouyang, Y., 2019. In situ LA-ICP-MS U-Pb geochronology and trace element analysis of hydrothermal titanite from the giant Zhuxi W (Cu) skarn deposit South China. Mineralium Deposita. 54, 569–590. https://doi.org/10.1007/s00126-018-0831-3.
Stein, H., Scherstén, A., Hannah, J., Markey, R., 2003. Subgrain-scale decoupling of Re and 187Os and assessment of laser ablation ICP-MS spot dating in molybdenite. Geochim. Cosmochim. Acta 67, 3673–3686. https://doi.org/10.1016/s0016-7037(03)00269-2.
Subarkah, D., Blades, M.L., Collins, A.S., Farkaš, J., Gilbert, S., Löhr, S.C., Redaa, A., Cassidy, E., Zack, T., 2022. Unraveling the histories of Proterozoic shales through in situ Rb-Sr dating and trace element laser ablation analysis. Geology 50, 66–70. https://doi.org/10.1130/g49187.1.
Sugiyama, N., Shikamori, Y., 2015. Removal of spectral interferences on noble metal elements using MS/MS reaction cell mode of a triple quadrupole ICP-MS. J. Anal. at. Spectrom. 30, 2481–2487. https://doi.org/10.1039/c5ja00308c.
Suoranta, T., Bokhari, S.N.H., Meisel, T., Niemelä, M., Perämäki, P., 2016. Elimination of interferences in the determination of palladium, platinum and rhodium mass fractions in moss samples using ICP-MS/MS. Geostand. Geoanal. Res. 40, 559–569. https://doi.org/10.1111/ggr.12116.
Tanner, S.D., Baranov, V.I., Bandura, D.R., 2002. Reaction cells and collision cells for ICP-MS: a tutorial review. Spectrochim. Acta - Part B at. Spectroscopy. 57, 1361–1452. https://doi.org/10.1016/S0584-8547(02)00069-1.
Tillberg, M., Drake, H., Zack, T., Hogmalm, J., Åström, M., 2017. In situ Rb-Sr dating of fine-grained vein mineralizations using LA-ICP-MS. Procedia Earth Planet. Sci. 17, 464–467. https://doi.org/10.1016/j.proeps.2016.12.117.
Tillberg, M., Drake, H., Zack, T., Kooijman, E., Whitehouse, M.J., Astrom, M.E., 2020. In situ Rb-Sr dating of slickenfibres in deep crystalline basement faults. Sci. Rep. 10, 562. https://doi.org/10.1038/s41598-019-57262-5.
Tillberg, M., Drake, H., Zack, T., Hogmalm, J., Kooijman, E., Åström, M., 2021. Reconstructing craton-scale tectonic events via in situ Rb-Sr geochronology of polyphased vein mineralization. Terra Nova 33, 502–510. https://doi.org/10.1111/ter.12542.
van Doncen, M., Weinberg, R.F., Tomkins, A.G., 2010. REE-Y Ti, and P remobilization in magmatic rocks by hydrothermal alteration. during Cu-Au deposit formation. Econ. Geol. 105, 763–776. https://doi.org/10.2113/gsecongeo.105.4.763.
Verschure, R.H., Andriessen, P.A.M., Boelrijk, N.A.I.M., Hebeda, E.H., Maijer, C., Priem, H.N.A., Verdurmen, E.A.T., 1980. On the thermal stability of Rb-Sr and K-Ar biotite systems: evidence from coexisting Sveconorwegian (ca. 870 Ma) and Caledonian (ca 400 Ma) biotites from SW Norway. Contrib. Mineral. Petrol. 74, 245–252.
Wang, C., Alard, O., Lai, Y.-J., Foley, S.F., Liu, Y., Munnikhuis, J., Wang, Y., 2022. Advances in in-situ Rb-Sr dating using LA-ICP-MS/MS: applications to igneous rocks of all ages and to the identification of unrecognized metamorphic events. Chem. Geol. 610 https://doi.org/10.1016/j.chemgeo.2022.121073.
Webster, J.D., Duffield, W.A., 1994. Extreme halogen abundances in tin-rich magma of the Taylor Creek Rhyolite, New Mexico. Econ. Geol. 89, 840–850.
Weis, P., Driesner, T., Heinrich, C.A., 2012. Porphyry-copper ore shells form at stable pressure-temperature fronts within dynamic fluid plumes. Science 338, 1613–1616. https://doi.org/10.1126/science.1225009.
Wilkinson, C.C., Cooke, D.R., Baker, M.J., Wilkinson, J.J., 2020. Exploration targeting in porphyry Cu systems using propylitic mineral chemistry: A case study of the El Teniente Deposit, Chile. Econ. Geol. 6, 917–925. https://doi.org/10.1038/NGEO1940.
Willigers, B.J.A., Mezger, K., Baker, J.A., 2004. Development of high precision Rb–Sr phlogopite and biotite geochronology; an alternative to 40Ar/39Ar tri-octahedral mica dating. Chem. Geol. 213, 339–358. https://doi.org/10.1016/j.chemgeo.2004.07.006.
Woods, G., 2014. Resolution of 176Yb and 176Lu interferences on 176Hf to enable accurate 176Hf/177Hf isotope ratio analysis using ICP-QQQ with MS/MS. Agilent Technologies, UK.
Wu, S., Zeng, X., Dai, X., Hu, Y., Li, G., Zheng, C., 2016. Accurate determination of ultra-trace impurities, including europium, in ultra-pure barium carbonate materials through inductively coupled plasma-tandem mass spectrometry. Spectrochim. Acta - Part B at. Spectroscopy. 123, 129–133.
Wu, S., Wang, H., Yang, Y., Niu, J., Lan, Z., Zhang, L., Huang, C., Xie, L., Xu, L., Yang, J., Wu, F., 2023. In situ Lu–Hf geochronology with LA-ICP-MS/MS analysis. J. Anal. at. Spectrom. 38, 1285–1300. https://doi.org/10.1039/d2ja00407k.
Xiang, D., Zhang, Z., Zack, T., Chew, D., Yang, Y., Wu, L., Hogmalm, J., 2021. Apatite U-Pb dating with common Pb correction using LA-ICP-MS/MS. Geostand. Geoanal. Res. 45, 621–642. https://doi.org/10.1111/ggr.12404.
Yamada, N. 2015. Feasibility study of fluorine detection by ICP-QQQ. Agilent 8800 ICP-QQQ Application Handbook, 2nd ed., Agilent Technologies: Santa Clara, CA. 38−39.
Yang, Z., Jackson, S.E., Cabri, L.J., Wee, P., Longerich, H.P., Pawlak, M., 2020. Quantitative determination of trace level (ng g(-1)) contents of rhodium and palladium in copper-rich minerals using LA-ICP-MS. J. Anal. at. Spectrom. 35, 534–547. https://doi.org/10.1039/c9ja00285e.
Zack, T., Hogmalm, J., 2015. In-situ Lu-Hf dating of xenotime by reaction cell isotope separation. Czech Republic, Goldschmidt, Prague.
Zack, T., Hogmalm, K.J., 2016. Laser ablation Rb/Sr dating by online chemical separation of Rb and Sr in an oxygen-filled reaction cell. Chem. Geol. 437, 120–133. https://doi.org/10.1016/j.chemgeo.2016.05.027.
Zhao, X.-Y., Zhong, H., Hu, R.-Z., Mao, W., Bai, Z.-J., Lan, T.-G., Xue, K., 2021. Evolution of multistage hydrothermal fluids in the Luoboling porphyry Cu-Mo deposit, Zijinshan ore field, Fujian Province, China: insights from LA-ICP-MS analyses of fluid inclusions. Econ. Geol. 116, 581–606. https://doi.org/10.5382/econgeo.4788.
Zhou, M., Li, M.Y.H., Wang, Z., Li, X., Liu, J., 2020. The genesis of regolith-hosted rare earth element and scandium deposits: Current understanding and outlook to future prospecting. Chinese Sci. Bull. 65, 3809–3824.
Zhu, Y., 2018. Classification of chemical elements in the reaction cell of ICP-MS based on the affinities with sulfur, oxygen, and fluorine. Chem. Lett. 47, 740–743. https://doi.org/10.1246/cl.180192.
Zhu, Y.B., Ariga, T., Nakano, K., Shikamori, Y., 2021. Trends and advances in inductively coupled plasma tandem quadruple mass spectrometry (ICP-QMS/QMS) with reaction cell. At. Spectrosc. 42, 299–309. https://doi.org/10.46770/AS.2021.710.
Zimmerman, A., Yang, G., Stein, H.J., Hannah, J.L., 2022. A critical review of molybdenite Re-187 parent-Os-187 daughter intra-crystalline decoupling in light of recent in situ micro- scale observations. Geostand. Geoanal. Res. 46, 761–772. https://doi.org/10.1111/ggr.12448.
Zwahlen, C., Cioldi, S., Wagner, T., Rey, R., Heinrich, C., 2014. The porphyry Cu-(Mo-Au) deposit at Altar (Argentina): Tracing gold distribution by vein mapping and LA-ICP-MS mineral analysis. Econ. Geol. 109, 1341–1358. https://doi.org/10.2113/econgeo.109.5.1341.